Icarus 302 (2018) 537–559

Contents lists available at ScienceDirect

Icarus

journal homepage: www.elsevier.com/locate/icarus

Planetary boundary layer and circulation dynamics at Gale Crater, Mars

Ricardo M. Fonseca[a,*], María-Paz Zorzano-Mier[a,b], Javier Martín-Torres[a,c]

[a] Division of Space Technology, Department of Computer Science, Electrical and Space Engineering, Luleå University of Technology, 971 87 Luleå, Sweden
[b] Centro de Astrobiología (INTA-CSIC), Torrejón de Ardoz, 28850 Madrid, Spain
[c] Instituto Andaluz de Ciencias de la Tierra (CSIC-UGR), 18100 Granada, Spain

ARTICLE INFO

Article history:
Received 20 February 2017
Revised 28 November 2017
Accepted 30 November 2017
Available online 6 December 2017

Keywords:
Mars
Atmosphere
Dynamics
Curiosity
Planetary boundary layer
MarsWRF

ABSTRACT

The Mars implementation of the Planet Weather Research and Forecasting (PlanetWRF) model, MarsWRF, is used here to simulate the atmospheric conditions at Gale Crater for different seasons during a period coincident with the Curiosity rover operations. The model is first evaluated with the existing single-point observations from the Rover Environmental Monitoring Station (REMS), and is then used to provide a larger scale interpretation of these unique measurements as well as to give complementary information where there are gaps in the measurements.

The variability of the planetary boundary layer depth may be a driver of the changes in the local dust and trace gas content within the crater. Our results show that the average time when the PBL height is deeper than the crater rim increases and decreases with the same rate and pattern as Curiosity's observations of the line-of-sight of dust within the crater and that the season when maximal (minimal) mixing is produced is L_s 225°–315° (L_s 90°–110°). Thus the diurnal and seasonal variability of the PBL depth seems to be the driver of the changes in the local dust content within the crater. A comparison with the available methane measurements suggests that changes in the PBL depth may also be one of the factors that accounts for the observed variability, with the model results pointing towards a local source to the north of the MSL site.

The interaction between regional and local flows at Gale Crater is also investigated assuming that the meridional wind, the dynamically important component of the horizontal wind at Gale, anomalies with respect to the daily mean can be approximated by a sinusoidal function as they typically oscillate between positive (south to north) and negative (north to south) values that correspond to upslope/downslope or downslope/upslope regimes along the crater rim and Mount Sharp slopes and the dichotomy boundary. The smallest magnitudes are found in the northern crater floor in a region that comprises Bradbury Landing, in particular at L_s 90° when they are less than 1 m s^{-1}, indicating very little lateral mixing with outside air. The largest amplitudes occur in the south-western portions of the crater where they can exceed 20 m s^{-1}. Should the slope flows along the crater rims interact with the dichotomy boundary flow, which is more likely at L_s 270° and very unlikely at L_s 90°, they are likely to interact constructively for a few hours from late evening to nighttime (~17–23 LMST) and from pre-dawn to early morning (~5–11 LMST) hours at the norther crater rim and destructively at night (~22–23 LMST) and in the morning (~10–11 LMST) at the southern crater rim.

We conclude that a better understanding of the PBL and circulation dynamics has important implications for the variability of the concentration of dust, non-condensable and trace gases at the bottom of other craters on Mars as mixing with outside air can be achieved vertically, through changes in the PBL depth, and laterally, by the transport of air into and out of the crater.

© 2017 The Authors. Published by Elsevier Inc.
This is an open access article under the CC BY-NC-ND license.
(http://creativecommons.org/licenses/by-nc-nd/4.0/)

* Corresponding author.
E-mail address: Ricardo.Fonseca@ltu.se (R.M. Fonseca).

https://doi.org/10.1016/j.icarus.2017.11.036
0019-1035/© 2017 The Authors. Published by Elsevier Inc. This is an open access article under the CC BY-NC-ND license. (http://creativecommons.org/licenses/by-nc-nd/4.0/)

1. Introduction

The Planetary Boundary Layer (hereafter PBL) is the part of the atmosphere closest to the surface, within which the interactions between the atmosphere and the surface take place. On Mars it is in this region where dust is lifted and settles back to the surface, where water and other trace molecules may be transferred between the surface and the atmosphere, and where turbulence and small-scale features such as convective vortices and topographic flows occur (Petrosyan et al., 2011). Dust is a fundamental component of the atmosphere on Mars that has a strong impact on its thermal and dynamical state. It affects the operation of surface spacecraft as well as the retrieval from orbiters and it is also critical for the entry, descent and landing phase of surface spacecraft probes. Despite its central importance, to date the circulation within this region of the atmosphere has been poorly validated due to the scarcity of in-situ instruments on the surface of Mars. The goal of this work is to investigate the PBL and circulation dynamics on daily and seasonal time-scales to better understand their variability and potential implications for: (1) the concentration of trace gases such as methane; (2) the dynamics of dust, and; (3) the interaction between regional and local slope flows. The Martian implementation of the Mars Weather Research and Forecasting (MarsWRF) model (Richardson et al., 2007) is used here to simulate the atmospheric conditions at Gale Crater for different seasons during a period coincident with the Curiosity rover operations. The model will be first validated with the existing single-point observations from Curiosity, and will then be used to provide a larger scale interpretation of these unique measurements as well as to provide complementary information where there are gaps in measurements.

On August 6th 2012 (UTC), the Mars Science Laboratory (MSL) mission successfully landed and delivered the rover Curiosity to the surface on Mars at 4.49°S, 137.42°E, in the north-western part of Gale Crater, a 154 km wide crater located at the edge of the hemispheric dichotomy, whose floor is at 4.451 km below datum. The central mound of Aeolis Mons (Mount Sharp) rises about 5.5 km above the floor of the crater (Anderson and Bell, 2010). Gale is an impact crater that is estimated to have formed ~3.6–3.8 billion years ago (Thompson et al., 2011). On board the MSL rover is the Rover Environmental Monitoring Station (REMS; Gómez-Elvira et al., 2012, 2014) which comprises several sensors including air and ground temperature sensors, a pressure sensor, an ultraviolet (hereafter UV) sensor with 6 detectors and a wind sensor. Being the only surface observation station in the region (and one of only two rovers currently operating on the planet), REMS measurements have proven to be very useful and have been used for a wide variety of purposes including to gain further insight into the properties of some of the soil types present on Mars (e.g. Martínez et al., 2014; Hamilton et al., 2014), to perform dust (Moore et al., 2016), moisture (Savijärvi et al., 2015) and pressure (Haberle et al., 2014; Ullán et al., 2017) studies and to investigate the chemical composition of the surface and subsurface and the possible viability of transient liquid water (Martín-Torres et al., 2015). This dataset has also been used to evaluate the performance of numerical models (e.g. Pla-García et al., 2016; Rafkin et al., 2016) that investigate the influence of the atmospheric circulation dynamics on local scales. More recently, in Newman et al. (2017) REMS data have been used to verify the performance of MarsWRF during the season of the Bagnold Dunes Campaign, as well as to constrain the setup and assumptions used in the model.

A discussion of the meteorological conditions at Gale is given in Rafkin et al. (2016). Outside the dust storm season (which typically begins around L_s 180°–225° and ends around L_s 315°–360°; L_s is the areocentric solar longitude) the circulation at Gale is dominated by upslope (downslope) flows along Mount Sharp and the crater rim during the day (night). In the daytime the winds diverge from the bottom of the crater and converge higher up with descent in the middle of the crater which acts to suppress convection and reduce the depth of the boundary layer (Tyler and Barnes, 2013; Moores et al., 2015). At night the downslope winds do not typically reach the bottom of the crater as at some point in their descent the compressed air parcels will be warmer than the air below and hence will lose their negative buoyancy. At this point they flow horizontally, gliding over the colder air below and forming katabatic sheets. As a result, the air at the bottom of the crater remains largely isolated with very little mixing with the outside air. In the dust storm season these local circulations are likely to be disrupted by the global mean meridional circulation: the large-scale northerly winds favour the downslope flow along the northern crater rim leading to strong mixing with the air from outside the crater in what is known as a "flushing" event (Rafkin et al., 2016). The global mean meridional circulation is stronger in the austral summer primarily due to: (i) the asymmetry in the solar insolation (in the austral summer the insolation is up to 45% greater than in the boreal summer leading to a stronger Hadley circulation; Zurek et al., 1992); (ii) the hemispheric dichotomy (as the northern one-third of Mars is at a lower elevation than the bottom two-thirds of the planet, in the boreal winter the lower surface temperatures in the northern polar region lead to higher surface pressures that together with the elevated terrain in the southern hemisphere and associated lower surface pressures enhance the global mean meridional circulation (Hourdin et al., 1993; Joshi et al., 1995; Richardson and Wilson, 2002); and (iii) the increased amount of dust in the atmosphere in the austral summer compared to the boreal summer that acts as a positive feedback strengthening the Hadley cell (Forget et al., 1999).

In this paper, a Martian atmospheric numerical model is run for Gale Crater with the model performance evaluated against observational data given by REMS. The primary focus is on the diurnal cycle of the PBL depth in the different seasons during a Martian year. Since the landing of Curiosity at Gale Crater, REMS, the Navigation Cameras (Navcam) and Mastcam have provided two and a half Martian Years (MY, the convention of Clancy et al. (2000) is used in this work) of observations of the Martian dust cycle from the surface (Moore et al., 2016). We hypothesize that the PBL height variability may be the driver of the dust content variability within the crater as well as of the variability of other trace molecules such as methane, which has been measured with variable concentration during the year at the crater floor (Webster et al., 2013, 2015). As we shall see in this work, even if the maximum depth of the PBL exceeds the height of the crater rim, vertical mixing with the outside air will be limited by the period of time during which it is deeper than this height (i.e. the temporal extension of the daytime convective boundary layer). Another topic discussed here is circulation dynamics, with a focus on the interaction between the crater slope flows and the regional-scale flows. While variations in the PBL depth will affect the extent of the vertical mixing of the air inside the crater with that outside, changes in the horizontal circulation will determine the amount of lateral transport of air into and out of the crater. By accounting for the full three-dimension circulation, further insight into the variability of dust and trace gases such as methane can be gained. In addition to the global mean meridional circulation (which is expected to impart southerly winds around L_s 90°, northerly winds around L_s 270° and weak and variable winds at the equinoxes), the circulation at Gale is controlled by local slope flows and regional slope flows. The latter, and besides the dichotomy boundary flow (which is expected to be significant as Gale is located at the edge of the hemispheric dichotomy), includes slope flows from neighbouring topographic features such as Elysium Mons located to the north. The local and regional slope flows generally blow

Table 1
Data sources for the topography, surface albedo and thermal inertia used in the MarsWRF's experiments.

Model Parameter	Data Source	Reference
Topography	Mars Orbiter Laser Altimeter (MOLA) 1/64° topographic grid	Smith et al. (2001)
Surface Albedo	Thermal Emission Spectrometer (TES) MY26 albedo map	Putzig and Mellon (2007)
Thermal Inertia	Thermal Emission Spectrometer (TES) apparent thermal inertia nightside map	Putzig and Mellon (2007)

upslope during daytime and downslope at night and, as discussed in Tyler and Barnes (2013), can interact constructively or destructively. In Tyler and Barnes (2013), however, the potential interaction between the slope flows along the crater rims and the dichotomy boundary flow is only considered for one season (L_s 151°) and a specification of the times when it may occur has not been stated. A better understanding of this interaction is crucial as advection by the wind has been shown to play a very important role in the variability of trace gases such as methane (Mischna et al., 2011; Viscardy et al., 2016). Given the strong topographic contrasts that exist everywhere on Mars, insight gained from this work is applicable to other places on Mars, in particular to craters and features with a similar topography to Gale.

Section 2 provides details about the model setup and methods used. The results of the MarsWRF experiments are shown in Section 3. In Section 4 the focus is on circulation dynamics while in Section 5 the emphasis is on the variability of the boundary layer depth. A discussion of the main findings is presented in Section 6.

2. Experimental setup

In this study we use MarsWRF version 3.3.1. The model's grid and dynamical core, as well as most of the physical parameterization schemes, are described in Richardson et al. (2007) with further details provided in Toigo et al. (2012); Newman and Richardson (2015) and Newman et al. (2017). The model's topography, surface albedo and thermal inertia are derived from Mars Global Surveyor (MGS) measurements and their detailed references are provided in Table 1. A simplified CO_2 microphysics scheme is used, which accounts for the deposition and sublimation of CO_2 and assumes that all CO_2 condensed is directly deposited onto the surface. The total CO_2 inventory and albedo and emissivity of the north and south seasonal caps are tuned to produce an annual pressure cycle that best fits the Viking Lander 1 and 2 pressure curves (Guo et al., 2009). Thermal conduction within the subsurface is represented in the model by a 15-layer implicit scheme. The model does not have a permanent CO_2 ice cap at the southern pole but the effects of this residual cap are represented by keeping the ground temperatures at latitudes below 82.5°S equal to the frost temperature of CO_2 (Richardson and Wilson, 2002). The PBL parameterization scheme applied in the model is the Medium Range Forecast (MRF; Hong and Pan, 1996) PBL scheme. This scheme was first used in the MRF model (and hence it is called the MRF PBL scheme) and includes both local and non-local mixing. The PBL depth in the MRF scheme is determined as the first level starting from the surface at which the bulk Richardson number exceeds 0.5.

MarsWRF is run with a yearly repeatable dust distribution taken from the Mars Climate Database (MCD) "MGS dust scenario" (Montmessin et al., 2004; Toigo et al., 2012). The dust mixing ratio is assumed to be constant from the surface to a (spatially and temporally varying) height z_{max}, shown in Fig. 1(a), above which it rapidly declines (Conrath, 1975). Fig. 1(b) shows the seasonal and latitudinal distribution of the dust optical depth normalised to 7 hPa used as proxy for atmospheric opacity in the visible band in the model. The dust opacity increases during the dust storm season from L_s 180° to L_s 240° and starts to decrease just before the austral summer solstice with very little variability from L_s 0° to L_s 180°. The radiation scheme used is a k-distribution radiative transfer model (KDM) described in Mischna et al. (2012). A Non-Local Thermodynamic Equilibrium (NLTE) adjustment to the long-wave radiation flux based on López-Valverde et al. (2000) is also employed. At high-latitudes polewards of 70°, in order to prevent the use of a smaller time-step given by the decreasing zonal grid spacing with latitude, a zonal filter that damps high frequency waves is used (Richardson et al., 2007). In the top 4 km Rayleigh damping is applied to the three wind components and potential temperature on a time-scale of 100 s (Skamarock et al., 2008). In the global domain the zonal mean of the horizontal wind components and potential temperature is also damped in the top 3 model levels on time-scales of 2, 6, and 18 days, respectively, to zero for the wind components and 140 K for the temperature.

Table 2
Height above ground level of the MarsWRF GCM vertical layer centres. A scale height of 10 km is used in the computation of the heights.

Layer Number	Height (km)	Layer Number	Height (km)
1	0.112	24	7.386
2	0.339	25	7.862
3	0.572	26	8.362
4	0.810	27	8.889
5	1.054	28	9.445
6	1.304	29	10.033
7	1.560	30	10.658
8	1.823	31	11.325
9	2.093	32	12.040
10	2.371	33	12.809
11	2.657	34	13.643
12	2.951	35	14.553
13	3.254	36	15.554
14	3.567	37	16.666
15	3.889	38	17.917
16	4.223	39	19.348
17	4.568	40	21.019
18	4.925	41	23.025
19	5.295	42	25.538
20	5.680	43	28.903
21	6.080	44	34.010
22	6.497	45	44.993
23	6.931		

The model is set up in a five nested grid configuration with the domains shown in Fig. 2. The outermost grid is global at a horizontal resolution of 2° × 2° (~118.33 km) with the other domains centred on Gale Crater with horizontal resolutions of about 39.44 km, 13.15 km, 4.38 km, and 1.46 km. This domain configuration is nearly identical to that used in Newman et al. (2017), which also included a 6th domain at a resolution of 480 m. However, while in the referred paper the authors run the first two grids in hydrostatic mode and the remaining four in non-hydrostatic mode (Claire Newman, pers. comm., 2017), here only the global grid is run hydrostatically. In the vertical 45 levels, concentrated in the PBL region, are used with the model top at 120 km. A model top above an altitude of 90 km is needed for the model to properly simulate the global mean meridional circulation (Wilson, 1997; Forget et al., 1999). The approximate height above ground surface of the centre of the vertical layers is given in Table 2. The outermost (global) grid is first run for two Martian Years (MY, the

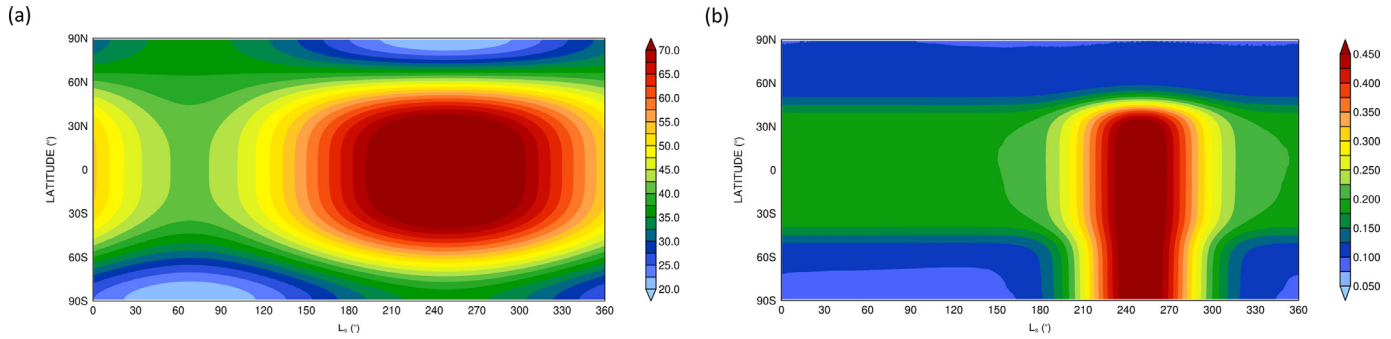

Fig. 1. Seasonal and latitudinal distribution of the (a) dust "top" (units of km) and (b) dust optical depth normalised to 7 hPa, used as proxy for atmospheric opacity in the visible band in the model, for the "MCD MGS" dust scenario.

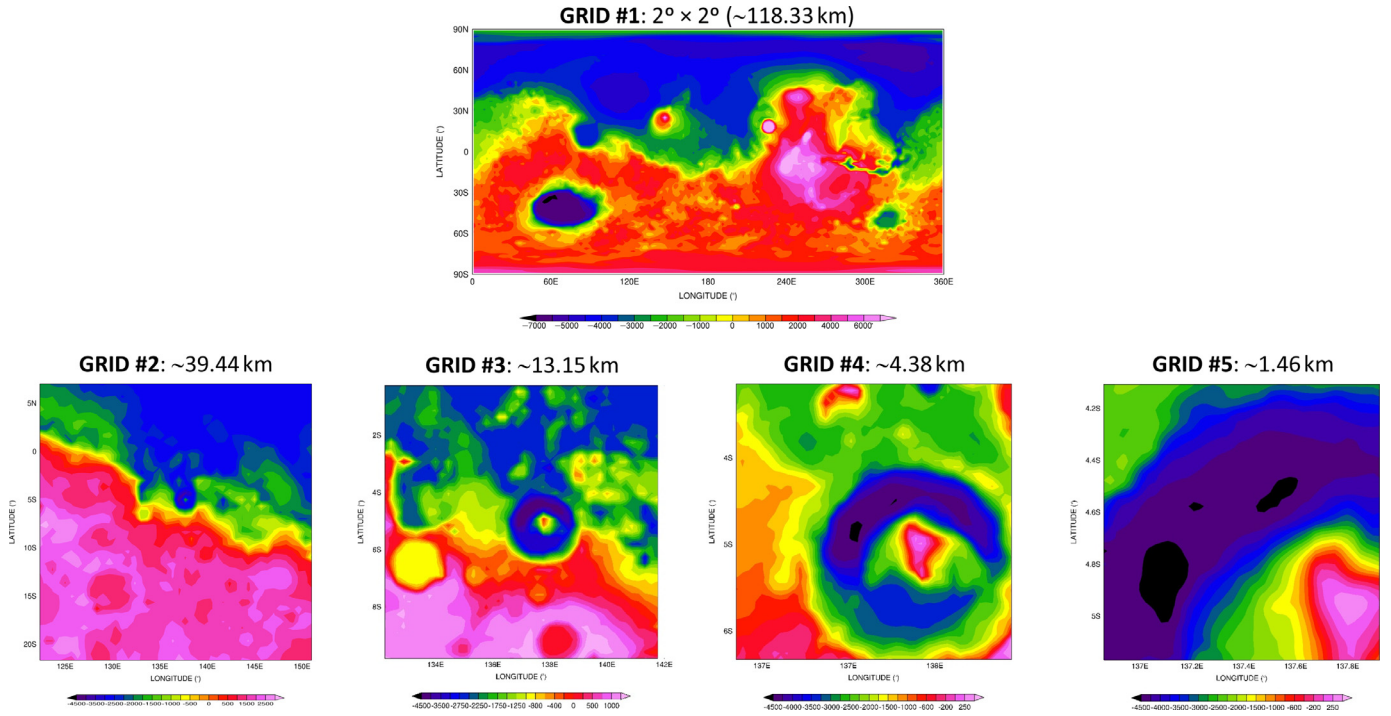

Fig. 2. Orography (units of meters) of the 5 grids used in the MarsWRF experiments. The outermost domain is global at a horizontal resolution of 2°×2°. The other grids are centred on the Gale Crater (the boundary regions are not shown here). The horizontal resolution of each domain is given above the correspondent plot.

convention of Clancy et al. (2000) is used in this work), MY31 and 32, with the first year regarded as model spin-up. Restart files are generated and stored every 10 sols and are subsequently used to initialize the nested experiments. The model is run in a 5-nest configuration for 7 sols (with a one-sol spin-up before) for about every 45° of solar longitude, including around the equinoxes and solstices, in order to properly sample the annual cycle: L_s 0° (REMS/MSL sols 354–360), L_s 45° (REMS/MSL sols 436–442), L_s 90° (REMS/MSL sols 546–552), L_s 148° (REMS/MSL sols 663–669), L_s 180° (REMS/MSL sols 726–732), L_s 225° (REMS/MSL sols 795–801), L_s 270° (REMS/MSL sols 865–871) and L_s 315° (REMS/MSL sols 934–940). It is important to note that L_s 148° is chosen instead of L_s 135° as in REMS/MSL sol 664 there was an unusually high number of convective vortices (Kahanpää et al. 2016) so it is of interest to run the model for this period. According to Moore et al. (2016), the amount of dust in the lower layers of the atmosphere (i.e. the line-of-sight opacity) at Gale is observed to be near a minimum around L_s 110° and a maximum around L_s 315°. As variability in boundary layer dynamics may be one of the drivers of the referred changes in dust mixing ratio, MarsWRF is also run for L_s 110° (REMS/MSL sols 586–592). All the aforementioned sols are within the first 1000 REMS/MSL sols, which will enable a comparison of the model output with REMS measurements. A time-step of 1 min is used for the outermost grid and for the four inner nests the time-steps used are 20 s, 10/3 s, 10/9 s and 10/27 s, respectively. For all experiments the model output is stored every 1 h for the first four grids and every 5 min for the innermost grid with the latter used for comparison with REMS data.

The REMS measurements used in this work are publicly available and documented at the National Aeronautics and Space Administration (NASA) Planetary Atmospheres Node of the Planetary Data System (PDS, http://pds-atmospheres.nmsu.edu/; Gómez-Elvira, 2013). The booms of REMS (in which the air and ground temperature and the wind sensors are found) are located at the mast of the rover approximately 1.6 m above ground level. Hence, the model's 1.5 m temperature and horizontal wind, extrapolated from the values at the surface and first model-level using the surface layer similarity theory (Newman et al., 2017; Jiménez et al., 2012), are compared with the corresponding REMS measurements. The MarsWRF's surface skin temperature is verified against the

REMS ground temperature while the model's surface pressure is evaluated against the observed pressure measurements. More information about REMS data can be found in Gómez-Elvira et al. (2012, 2014).

3. Model experiments

In this section a discussion of the results of the MarsWRF experiments is presented. The outputs of the model are compared with the REMS ground-truth observations for six seasons: austral winter (L_s 90°) and summer (L_s 270°) solstices and spring (L_s 180°) and autumn (L_s 0°) equinoxes as well as L_s 110° and 315°. The model performance for the other seasons (L_s 45°, 148° and 225°) is similar and hence is not discussed here.

3.1. Surface pressure

In Fig. 3 the results for the surface pressure are shown. The black circles show seven sols of the 5 min MarsWRF data for the closest model grid-point to the rover's location while the coloured circles show REMS measurements for seven sols (first sol in light blue, last in red) at the corresponding season. It is important to note that no observational data are available for REMS/MSL sols 359 and 360 (L_s 0°) and 938 (L_s 315°).

The daily mean surface pressure predicted by MarsWRF is similar to that observed, as given by REMS, for the sols of most of the experiments except for those of L_s 0° for which it is higher in the model. Higher than observed daily mean surface pressures at L_s 0° are also seen at other locations on Mars such as at the Viking Lander 1 site (Fig. S1). Regarding the diurnal cycle of the surface pressure, the observed maximum at ~6–9 LMST and minimum at ~17–18 LMST are generally captured by MarsWRF but the overall phase is not well replicated. The most likely reason for this is an incorrect representation of the dust distribution: as discussed in Guzewich et al. (2016), deficiencies in the atmospheric dust loading (also in the vertical, the observed detached layers at 20–30 km and large diurnal variability (e.g. McCleese et al., 2010; Navarro et al., 2014) are not present in the prescribed dust scenario considered here) have an impact on the atmospheric tides which directly affect the diurnal cycle of the surface pressure. These discrepancies in the phase are also seen at the Viking Lander 1 site (Fig. S1) further confirming the likely role of the atmospheric opacity. Outside the dust storm season there are relative maxima at ~1–3 LMST and ~19–21 LMST. These extrema, likely associated with the interaction between the atmospheric tides and the local crater circulation (Wilson et al., 2017), are reproduced by the model at L_s 180° but not at L_s 90° and 110°.

3.2. Ground & air temperatures

In Figs. 4 and 5 the results for the ground and air temperatures are given. The uncertainty for the ground temperature used is that given in REMS data whereas for the air temperature it is assumed to be ±5 K, the worst accuracy of the air temperature sensor to determine local temperatures near the rover platform (Gómez-Elvira et al., 2014). In the REMS data there are two air temperature readings taken by the two air temperature sensors: one from boom 1 and another from boom 2. Notice however that the mast where the booms are attached to is heated by the Sun and the local air in the boundary layer of the platform is typically warmer than the free air. Thus the air temperature fluctuates during daytime between a maximum, which is sensitive to the mast temperature, and a minimum, which is the one that should be compared with the MarsWRF temperature and hence used here as REMS air temperature data.

The MarsWRF ground temperature is generally in agreement with that observed except at L_s 270° (and, to a lesser extent, at L_s 315°) when the model temperature is higher by about 10 K during the early to mid-afternoon hours. As the nighttime temperatures are reasonably well captured, the higher daytime temperatures are likely due to an incorrect simulation of the surface albedo which may be too low in the model. A comparison of the model's surface albedo and thermal inertia with that estimated from rover imagery and a 1-D surface-atmosphere thermal model by Vasavada et al. (2017) seems to confirm this hypothesis: while the model's thermal inertia at the grid-point closest to the location of the rover is within the 200–400 J m^{-2} K^{-1} $s^{-1/2}$ range predicted by Vasavada et al. (2017) for all seasons, the surface albedo values are only in agreement for L_s 0° - 225° (~0.17 – 0.20), they are lower for L_s 270° and 315° (~0.17 in the model as opposed to predicted values of ~0.25). In addition, while in the sols of the L_s 90°, 110° and 180° experiments the model temperatures increase at a slower rate in the morning compared to the REMS temperatures, in particular at L_s 315° the opposite is true with the REMS temperatures increasing at a slower rate compared to those predicted by MarsWRF. As discussed in Pla-Garcia et al. (2016), these discrepancies may be related to the topographic orientation that is not well captured by the model at this resolution (insufficient to properly resolve local slopes) in addition to an incorrect representation of the atmospheric dust loading and surface properties (including albedo and thermal inertia). It is also interesting to note that, on top of the background diurnal cycle of ground temperature, there is very little variability during the daytime but at night REMS data show large fluctuations of more 20 K in relatively short periods of time, in particular in some of the sols in L_s 90° and 180°. These fluctuations, not seen in the air temperature (Fig. 5) and also not captured by the model, are likely caused by the noise of the Ground Temperature Sensor (GTS) electronics (Gómez-Elvira et al., 2014).

As seen in Fig. 5, the model predicted air temperatures are generally within the observed range of values but during daytime tend to be on the lower end at L_s 90°, 110° and 180° and upper end at L_s 270°. Some of these biases are also present in the ground temperature (e.g. warmer daytime temperatures at L_s 270°, Fig. 4) while others, such as the cooler daytime temperatures at L_s 180°, are not and may be attributed to an incorrect representation of the atmospheric circulation (e.g. the afternoon superadiabatic lapse rate may be steeper in MarsWRF in the L_s 180° season) which require higher horizontal (and vertical) resolution to be fully simulated. In addition, there are high-frequency fluctuations in the REMS air temperature data mostly during daytime (likely due to turbulent eddies) which are not captured by the model.

3.3. Horizontal wind direction & speed

Figs. 6 and 7 show the results for the horizontal wind direction and speed. The error bars in the horizontal wind direction reflect the information available on the PDS website: the uncertainty is typically ±15° if the wind is blowing from the front of the rover and ±45° if it is blowing from the rear. This is because the rear-pointing wind sensor boom was lost on landing, thus winds coming from the rear of the rover are strongly perturbed by the Remote Sensing Mast (on which the front wind sensor boom is mounted) before they reach the remaining wind sensor (Gómez-Elvira et al., 2014; Newman et al., 2017). No information regarding the uncertainty of the horizontal wind speed is available on the PDS website so following Newman et al. (2017) a ± 20% uncertainty is considered. It is important to note that when the wind is blowing from the rear of the rover the wind speed cannot be retrieved, due to the perturbations of rear winds before they reach the sensor, as stated above. When comparing the wind direction

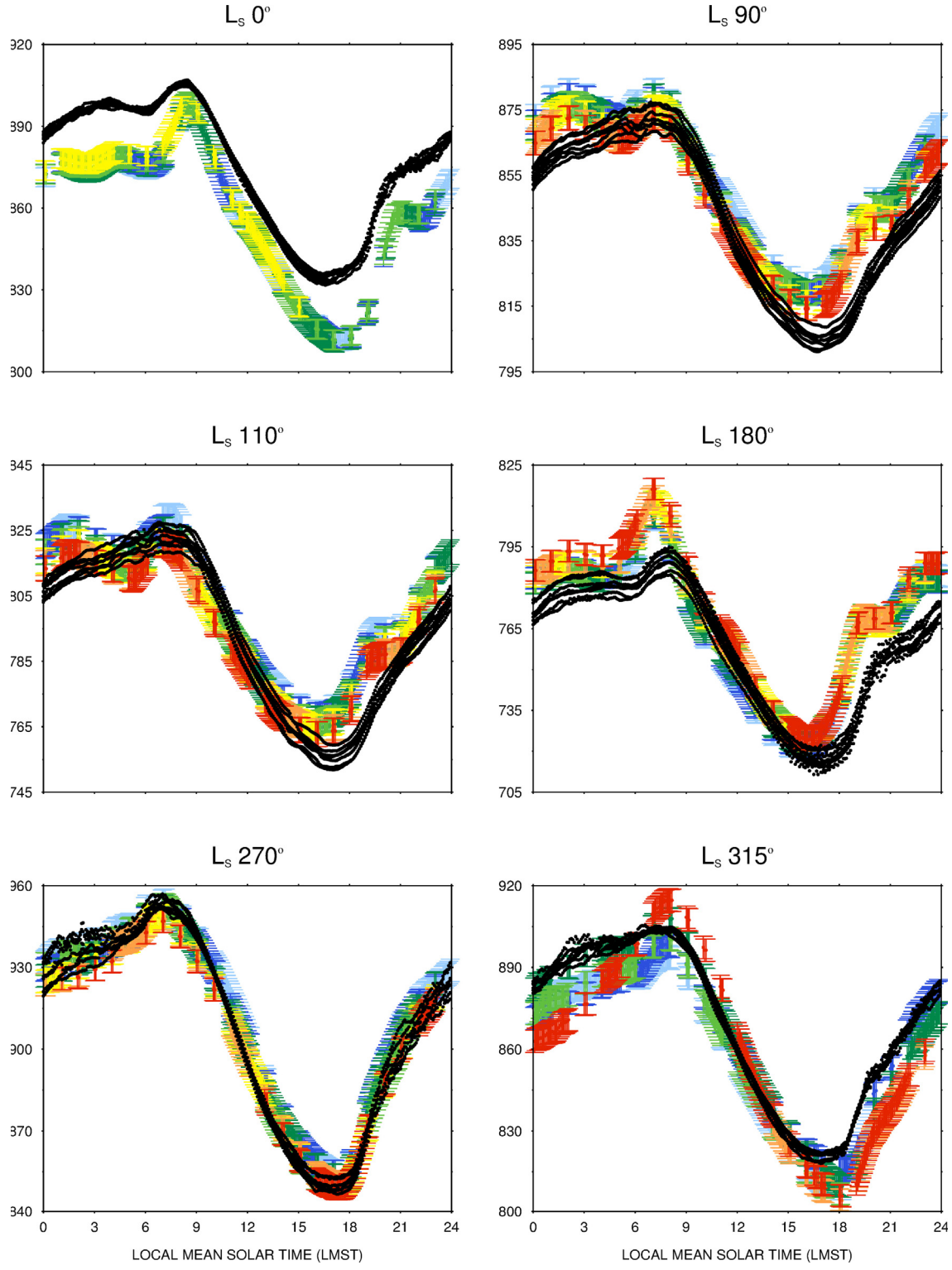

Fig. 3. WRF (black circles) and REMS (coloured circles with error bars) surface pressure (units of Pa) for REMS/MSL sols 354 to 360 (L_s 0°), 546 to 552 (L_s 90°), 586 to 592 (L_s 110°), 726 to 732 (L_s 180°), 865 to 871 (L_s 270°) and 934 to 940 (L_s 315°). For each season the REMS data points are coloured from blue (sol #1) to red (sol #7). Data for REMS/MSL sols 359 and 360 (L_s 0°) and 938 (L_s 315°) are not available. The WRF values are for the model grid-point closest to the location of the rover.

and speed with REMS measurements it is crucial to note that while observed winds are based on 5-min averages of instantaneous wind measurements taken at a single point, the MarsWRF winds are averaged over a grid-box at ~1.46 km horizontal resolution. The aforementioned issues with the REMS wind sensor mean that it is difficult to get clear picture of the observed winds. As the wind fields also typically exhibit a large spatial and temporal variability, a poorer match between model output and observations (compared to other variables such as surface pressure and air and ground temperatures) is to be expected, even if the model were to be relatively accurate.

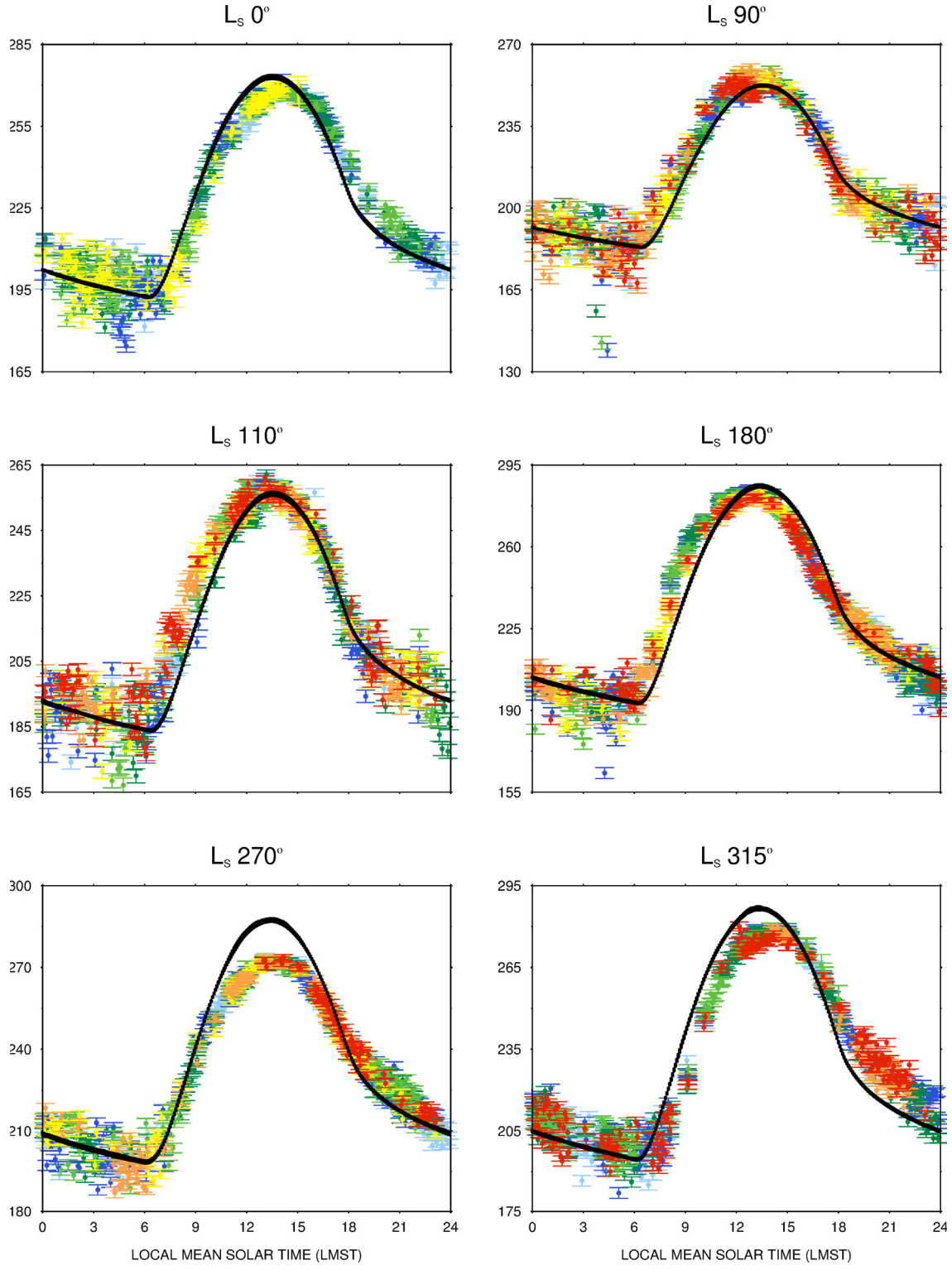

Fig. 4. As Fig. 3 but for the ground temperature (units of Kelvin).

Outside the dust storm season, and in particular at L_S 90° and 110°, the horizontal wind direction is more easterly from ~0 to 15 LMST, with a brief interlude with more variable directions from ~3 to 6 LMST, and exhibits a large variability in particular from the late afternoon to nighttime hours. These fluctuations, which take place mostly between 18 and 21 LMST (nighttime measurements are rare due to the wind sensor electronics limitation with temperature), are generally captured by the model. However, there are some southerly wind directions in mid-morning hours missed by MarsWRF. A possible explanation is that these winds arise from the influence of small-scale topography that is not resolved by the model. Regarding the wind speeds, and as seen in Fig. 7, there is good agreement in the early morning when the observed and modelled speeds are ~4–7 m s^{-1}, but in the afternoon and early evening the REMS wind speeds (~4–8 m s^{-1}) are much stronger than those predicted by MarsWRF (~0–2 m s^{-1}).

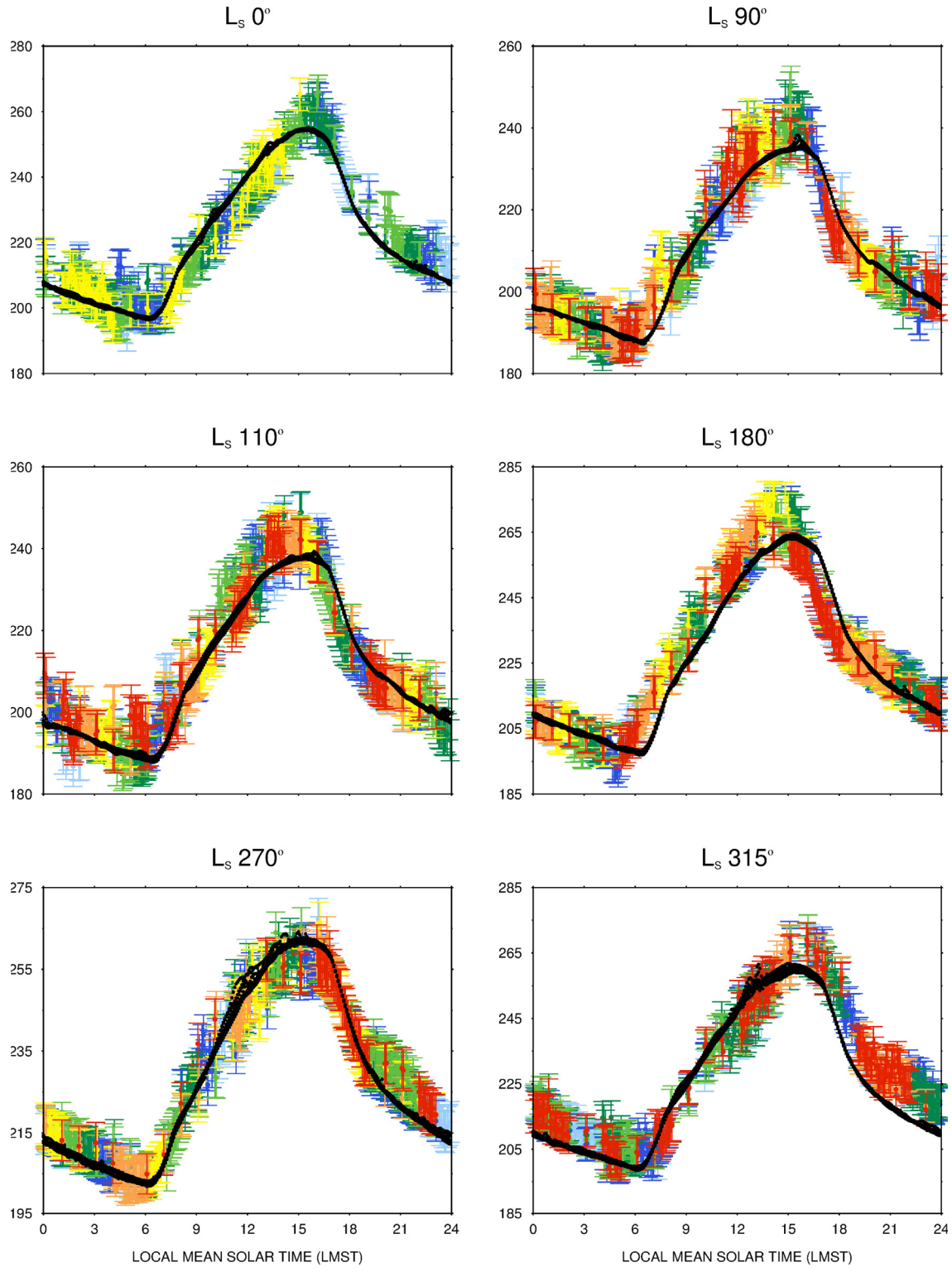

Fig. 5. As Fig. 3 but for the air temperature (units of Kelvin).

Newman et al. (2017) evaluated the performance of MarsWRF, considering different configurations, during the Bagnold Dunes Campaign which took place around L_s 90°. They found that by using a similar vertical resolution near the surface to that used in this work, the model is able to simulate the peak in the early morning winds but the late afternoon and evening winds are significantly under-estimated, as is the case here, whereas with a higher vertical resolution near the surface MarsWRF misses the early morning peak but simulates the higher evening wind speeds. In addition to the vertical resolution, the mismatch between the observed and modelled winds seen here can also be a result of deficiencies in the PBL scheme and insufficient horizontal resolution to properly resolve the topography (as discussed in Newman et al. (2017) topographic features can block winds blowing from a given direction) and surface properties. It is also important to stress that wind speed differences may also be attributed to the local character of

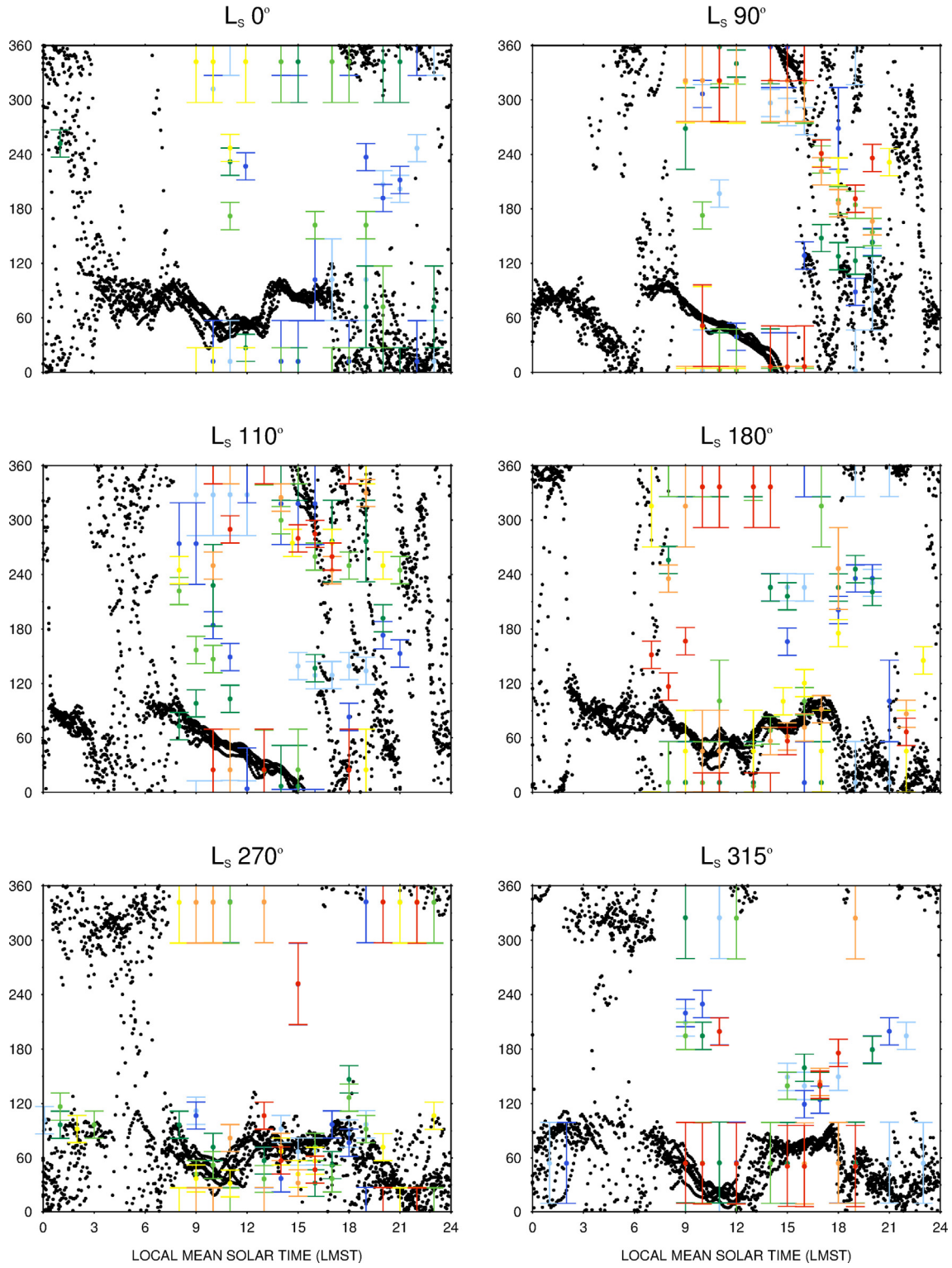

Fig. 6. As Fig. 3 but for the horizontal wind direction (units of °).

REMS wind speed retrieval and the perturbations induced by the platform rather than the MarsWRF model alone (Úllan et al., 2017). REMS was more able to measure the unobstructed wind at a wide range of times of day in some seasons than in others, depending on whether or not measurements were taken at a wide range of rover orientations (or at least at those which resulted in unobstructed winds). Thus in some seasons it is possible that the REMS dataset shown here does not reflect the complete wind field, and that the true dominant wind directions (and hence wind speeds) for a significant portion of the diurnal cycle were not measured. However, exploring this in detail would require an in-depth analysis of the complete wind dataset to locate periods when such a range of orientations were available, and is beyond the scope of this study.

During the dust storm season, in particular at L_s 270° and 315°, the local circulations at Gale are likely to be disrupted by

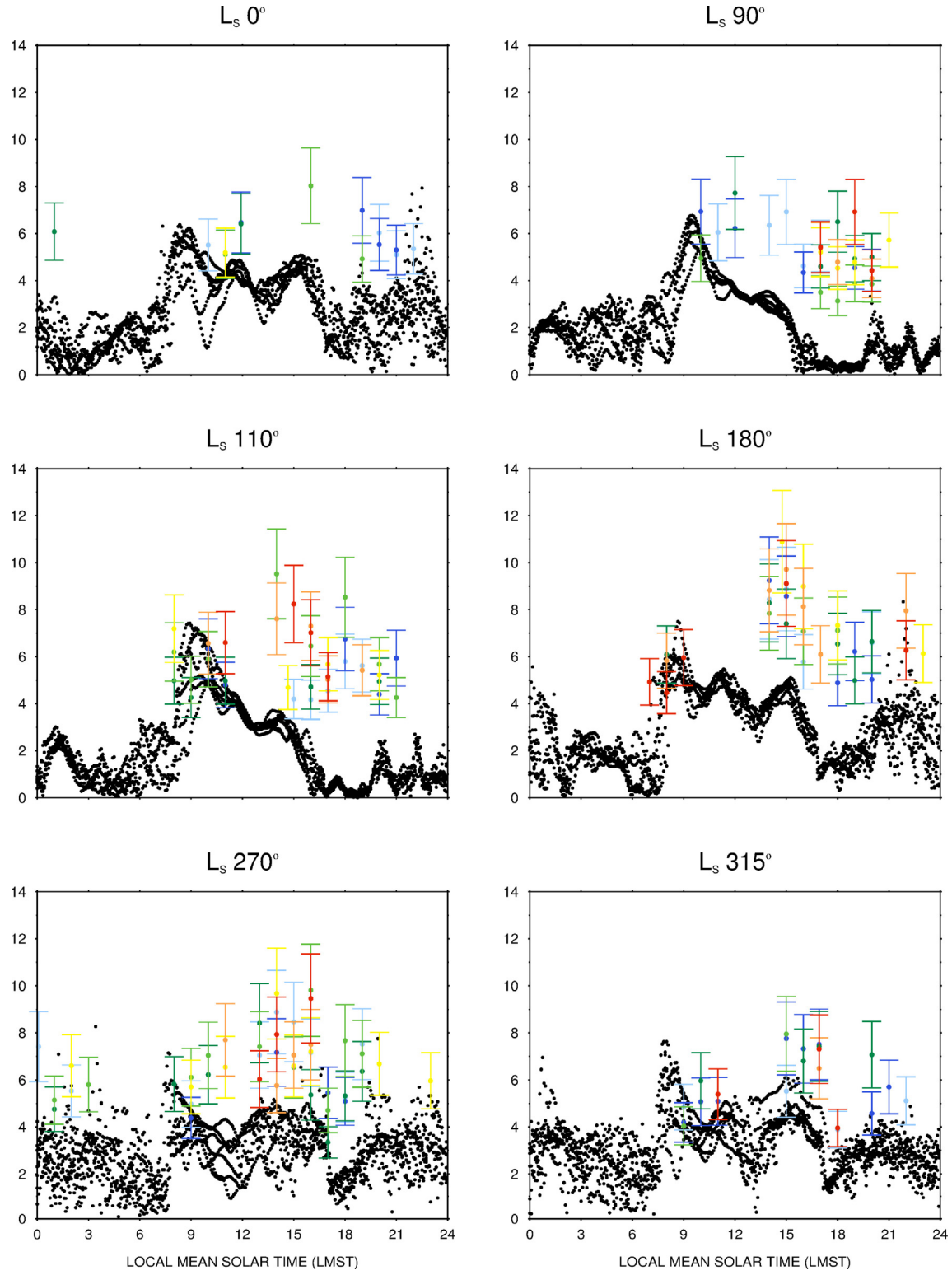

Fig. 7. As Fig. 3 but for the horizontal wind speed (units of m s^{-1}).

the global mean meridional circulation which will lead to more northerly winds at the crater floor (Rafkin et al., 2016). This is predicted by MarsWRF with wind directions predominantly from the east to north-west. While at L_s 270° there is a rather good agreement with REMS measurements, at L_s 315° there are several REMS observations of more southerly wind directions in the early morning (~9 LMST) and late afternoon and evening hours that are completely missed by the model. As these wind directions are present in all six seasons except L_s 270°, they are likely to be associated with more localized slope flows (with a possible contribution from the downslope winds from Mount Sharp) that are suppressed near the austral summer solstice when local circulation at Gale is disrupted. A higher spatial resolution would be needed to properly simulate these features. Regarding the wind speed, the warmer

temperatures at L_s 270° allow for some nighttime measurements that generally are of a similar magnitude to those given by the model which continues to underestimate the strength of the afternoon and early evening speeds. In the warm season the model also predicts larger inter-sol variability in the wind speed in particular during the daytime (~4 m s^{-1}, at L_s 90° the range is about 2 m s^{-1}).

In this section the focus has been on the L_s 0°, 90°, 110°, 180°, 270° and 315° seasons. However, similar results are obtained for the other seasons not discussed here (L_s 45°, 148° and 225°) in terms of surface pressure, ground and air temperatures and horizontal wind direction and speed (not shown). The L_s 148° experiment comprises REMS/MSL sol 664 during which a high number of convective vortices was observed at Gale Crater (Kahanpää et al., 2016). Ringrose et al. (2007) points out that convective vortices leave a signature on the wind fields (change in direction and speed), surface pressure (drop) and temperature (increase) with the latter only seen if the vortex passes overhead. MarsWRF does not show any of these "atypical" features in the 7 sols. This suggests that the observed dust devil burst was possibly related to dust storm activity, which is part of the intrinsic natural variability of the real system but is not part of the model's intrinsic variability because dust loading is prescribed. It is important to note that MarsWRF is run without data assimilation, an idealized dust distribution is used and even the albedo and thermal inertia maps employed are not those of MY32. Hence, if the dust devil burst was triggered by the passage of a dust front, as suggest by Kahanpää et al. (2016), the fact that it is not represented in the model means that MarsWRF will not be able to simulate the observed event.

4. Circulation dynamics

As discussed in Rafkin et al. (2016), the atmospheric circulation at Gale Crater is mostly the result of the interaction between the global mean meridional circulation (which leads to generally southerly/northerly winds around the austral winter/summer solstices and weak and variable winds at the equinoxes when the ascending branch of the Hadley cell crosses the equator), regional slope flows (which include the dichotomy boundary flow, expected to be significant as Gale is located near the edge of the hemispheric dichotomy, and flows from nearby topographic features such as the Elysium Mons to the north) and local crater slope flows (along the crater rim and the slopes of Mount Sharp). Even though the latter two flows are generally upslope during the day and downslope at night, the time of their maximum strength is not the same: as discussed in Tyler and Barnes (2013), their interaction can be both constructive and destructive. In this section the interaction between local (along the crater rim slopes) and regional (along the dichotomy boundary) flows at Gale Crater will be investigated.

For the two solsticial (L_s 90° and 270°) and equinoctial (L_s 0° and 180°) seasons the hourly diurnal cycle of the meridional wind, the dynamically important component of the horizontal wind field at Gale Crater (Tyler and Barnes, 2013), is obtained by averaging over the 7 sols with the daily-mean subtracted to remove the effects of the global mean meridional circulation. As the meridional wind tends to oscillate between the upslope and downslope regimes along the northern and southern crater rims, Mount Sharp slopes and the dichotomy boundary, its variation on a diurnal time-scale can be approximated by the least square method as a sinusoidal function of the form

$$V(t) = A\ cos[\omega(t-\phi)]$$

where A is the amplitude (in m s^{-1}), ϕ is the phase (defined as the time of maximum amplitude, in hours) and $\omega = 2\pi/24$h. Figs. 8 and 9 show the amplitude and phase, respectively, of the meridional wind at the first model level (~110 m) and for model grid #4 (horizontal resolution ~4.38 km). Bradbury Landing, highlighted by a cross in the plots, has one of the smallest meridional wind amplitudes anywhere in the crater ranging from ~0–1 m s^{-1} at L_s 90° (these extremely weak magnitudes suggest very little lateral mixing with outside air at this time of the year) to ~4–5 m s^{-1} at L_s 270°. The local minimum in meridional wind around the landing site has been reported in Tyler and Barnes (2013) and is expected as it corresponds to a deformation zone where the afternoon upslope flow diverges north up the crater rim and south up the slopes of Mount Sharp and the respective downslope flows converge at night. It is important to stress that even though here the fit is done to the meridional wind anomalies with respect to the daily mean, similar results are obtained with the full meridional wind indicating that the background (daily mean) wind is rather weak (not shown). The highest amplitudes are seen at the south-western parts of the crater extending into the western section of Mount Sharp (here, and in particular at L_s 90°, they exceed 20 m s^{-1}) and take place mostly around 4–6 LMST (given the sinusoidal function also around 16–18 LMST). The exception is at L_s 270° when the strongest meridional winds occur in portions of the northern crater rim, to the north-east of Bradbury Landing, mostly around 10–12 LMST. The results for the phase at Bradbury Landing at L_s 90°, and at other locations mostly in the northern crater floor at all seasons, have to be interpreted with care as the amplitude is rather small making it difficult to properly fit a sinusoidal function to the low magnitude oscillations in the meridional wind speed.

Figs. 10 and 11 show the time of transition between southerly and northerly wind regimes for model grids #4 (horizontal resolution ~4.38 km) and #2 (horizontal resolution ~39.44 km), respectively. As the meridional wind variation is approximated by a pure sinusoidal function, the transition from northerly to southerly wind regime will take place 12 h later. These transition times are determined by setting $V(t) = 0$ and solving for t. It is important to note that while in the northern crater rim the winds generally blow from south to north during the day and from north to south at night, the opposite is true at the southern crater rim and at the northern slopes of Mount Sharp. Figs. 10 and 11 highlight some of the main circulation features in the region which include the flows along the crater rims of Gale and the slopes of Mount Sharp, the dichotomy boundary flow which transitions to upslope (north to south) at ~11–13 LMST and downslope (south to north) at ~23–01 LMST, as well as the flow along the slopes of Elysium Mons which becomes downslope (north to south) at ~20–22 LMST and upslope (south to north) at ~8–10 LMST.

For L_s 0°, 180° and 270°, the transition from daytime to nighttime regime at the northern Gale Crater floor to the north of Bradbury Landing takes place from mid to late-afternoon hours, ~15–17 LMST. To the north of Gale, where the dichotomy boundary flow is expected to play the largest role, the transition from southerly to northerly winds (here nighttime to daytime regime) occurs at ~11–13 LMST whereas the transition from northerly to southerly winds takes place 12 h later, around 23–01 LMST. Should the two flows interact with each other, for a few hours (~17–23 LMST) they are likely to interact constructively as they both blow from north to south. The time window during which the referred interaction is possible is shortened for L_s 270° (~19–23 LMST) as in this season the transition to nighttime regime at the northern crater rim occurs later around 18–19 LMST. The possible interaction between local and regional slope flows at Gale mentioned here is likely to take place at L_s 270° as during this season the air at the bottom of the crater is expected to be strongly mixed with the outside air (Rafkin et al., 2016) and very unlikely to occur at L_s 90° when the air at the bottom of the crater is expected to be largely isolated from the outside air (Newman et al., 2017; Rafkin et al., 2016). As stated before, the results at L_s 90° have to be interpreted

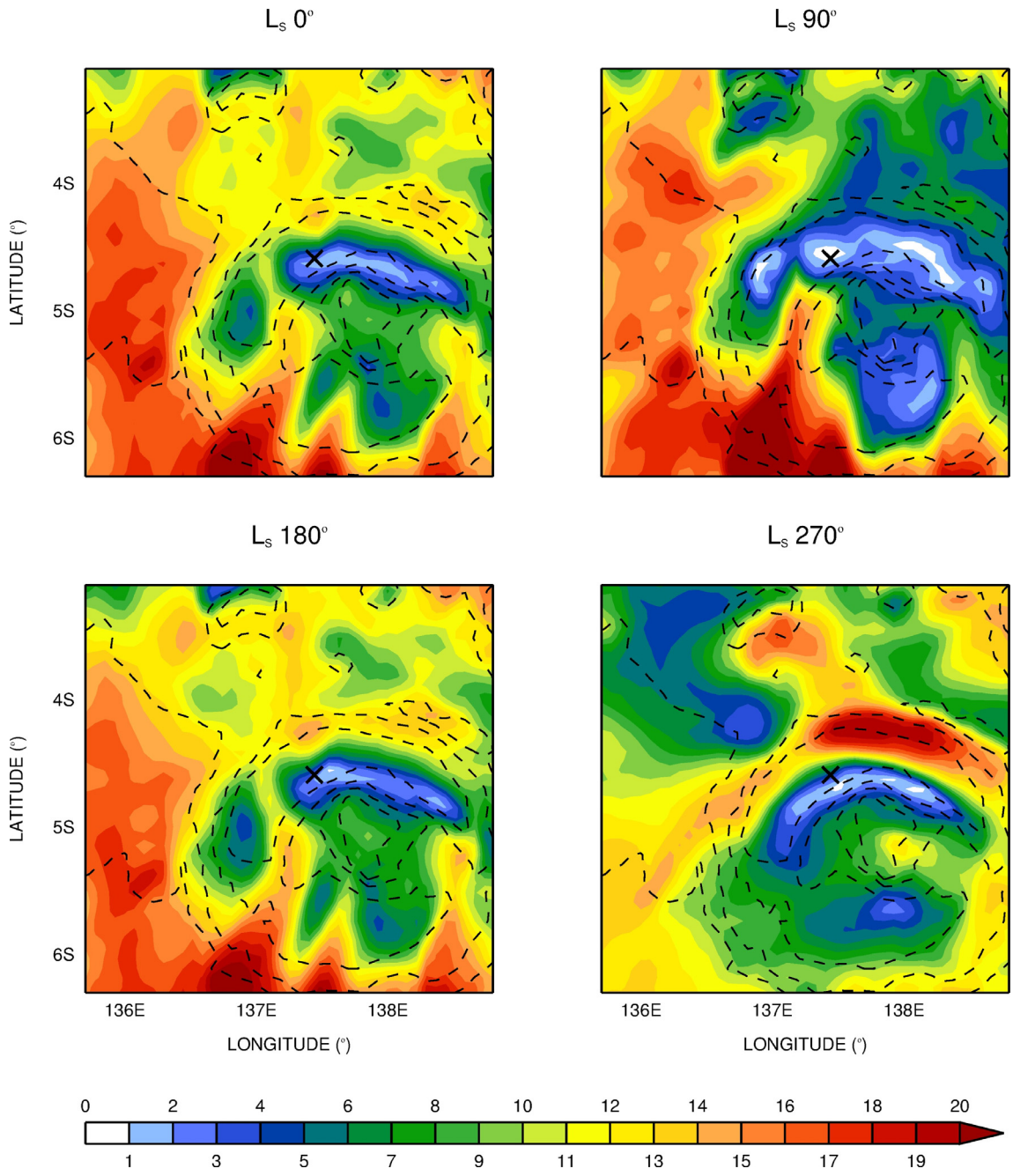

Fig. 8. Amplitude of the meridional wind, at the first model level (~110 m), anomalies with respect to the daily mean (units of m s^{-1}) for the sols of the L_s 0°, 90°, 180° and 270° experiments for model grid #4 (horizontal resolution ~4.38 km). The black lines are orography contours (negative contours are represented by dashed lines and positive contours by solid lines, the zero line is not shown) with a step of 1000 m. The black cross indicates the location of Bradbury Landing.

with care as a comparison with Fig. 8 reveals that in the same regions where in Fig. 10 there are blue shadings or a rapid change in the colour shading the amplitude of the meridional wind speed is rather small, less than 1 m s^{-1} in some locations, suggesting that the fit to a sinusoidal function may not work well. At the southern crater rim, and for all seasons, the transition from daytime (north to south) to nighttime (south to north) regime occurs at ~20–22 LMST, with the regional slope flow switching to downslope mode later around ~23–01 LMST. Should the two flows interact with each other in the period ~22–23LMST they will do so destructively as the slope flow along the crater rim has shifted to the south whereas the dichotomy boundary flow is still blowing from south to north. Similar results are obtained for the transition from nighttime to daytime regimes: at the northern section of the Gale Crater floor (including Bradbury Landing) this transition occurs from pre-dawn to early morning hours (~3–5 LMST) also earlier than further north away from the crater suggesting the possibility of a constructive interference between the regional slope flow (blowing from south to north) and the upslope flow along the northern crater rim from ~5–11 LMST. At the southern crater rim the local slope flow switches to daytime upslope mode also a few hours earlier than the regional slope flow suggesting should the two flows interact they will do so destructively from ~10–11 LMST. Here in the night to early morning (~1–8 LMST) and late morning to early evening (~13–20 LMST) hours the two flows are both downslope and upslope, respectively, meaning that they may

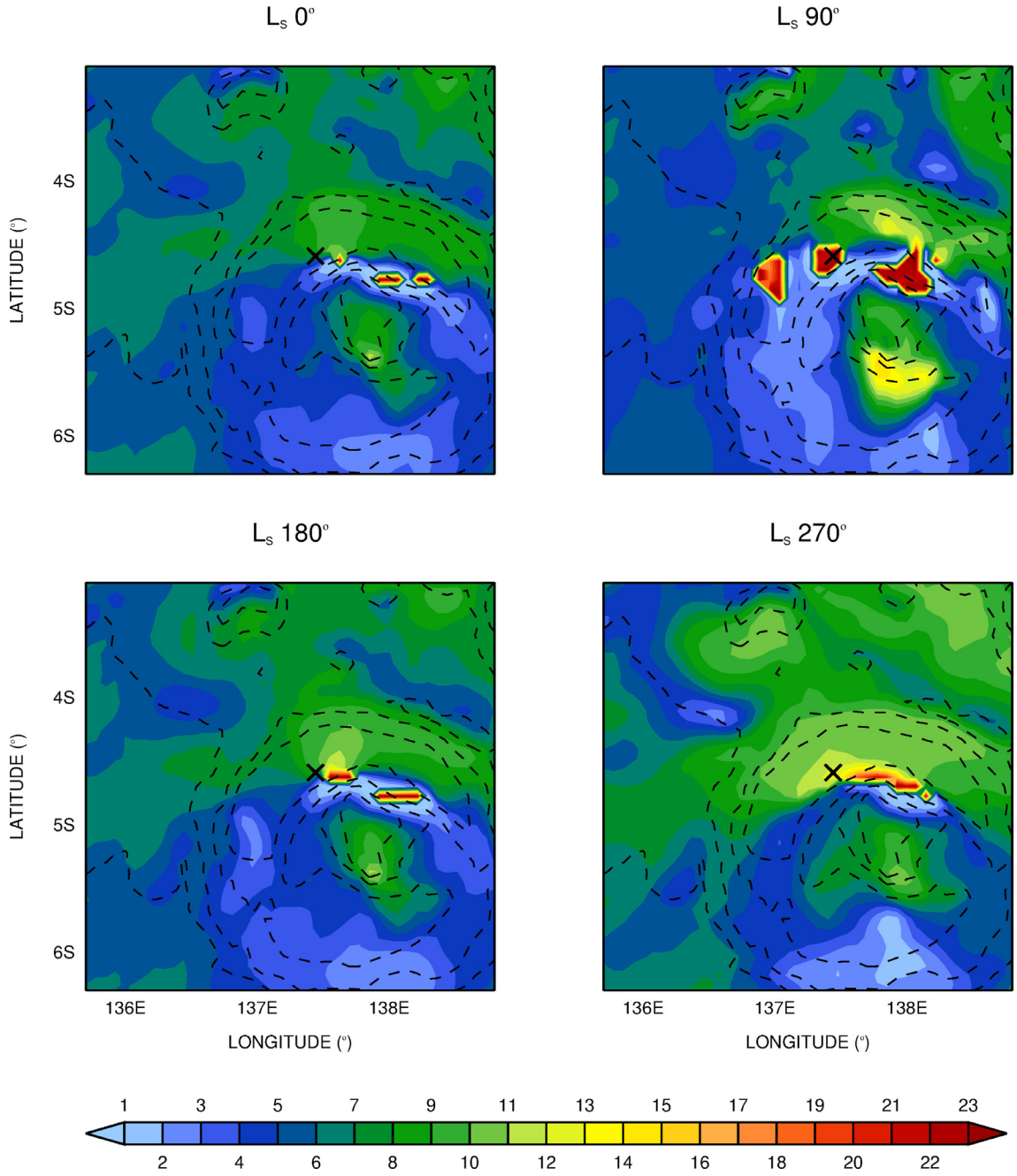

Fig. 9. As Fig. 8 but for the phase (time of maximum amplitude in LMST).

reinforce each other. The results in Figs. 10 and 11 indicate that for the L_s 0°, 180° and 270° seasons the local crater flows at the northern and southern crater rims switch from daytime/nighttime to nighttime/daytime regimes earlier than the regional slope flow which raises the possibility of constructive interaction between the slope flow at the northern crater rim and the dichotomy boundary flow from late afternoon to nighttime (~17–23 LMST) and from pre-dawn to early morning (~5–11 LMST) hours and destructive interaction at the southern crater rim at night (~22–23 LMST) and in the morning (~10–11 LMST). Further insight into the interaction between the slope flows along the crater rims and the dichotomy boundary flow can be achieved through semi-idealised experiments in which some of the topographic features, such as the dichotomy boundary, are smoothed out or even removed. Such experiments, which may provide further details as to when the referred interaction between the crater rim slope flows and the dichotomy boundary flow is likely to take place, will be left to a future paper.

5. Boundary layer dynamics

The variability of the PBL depth is investigated in this section. The results show that this element is the likely driver of changes in the local dust content within the crater. Possible implications for the variability of trace atmospheric elements such as methane are also discussed.

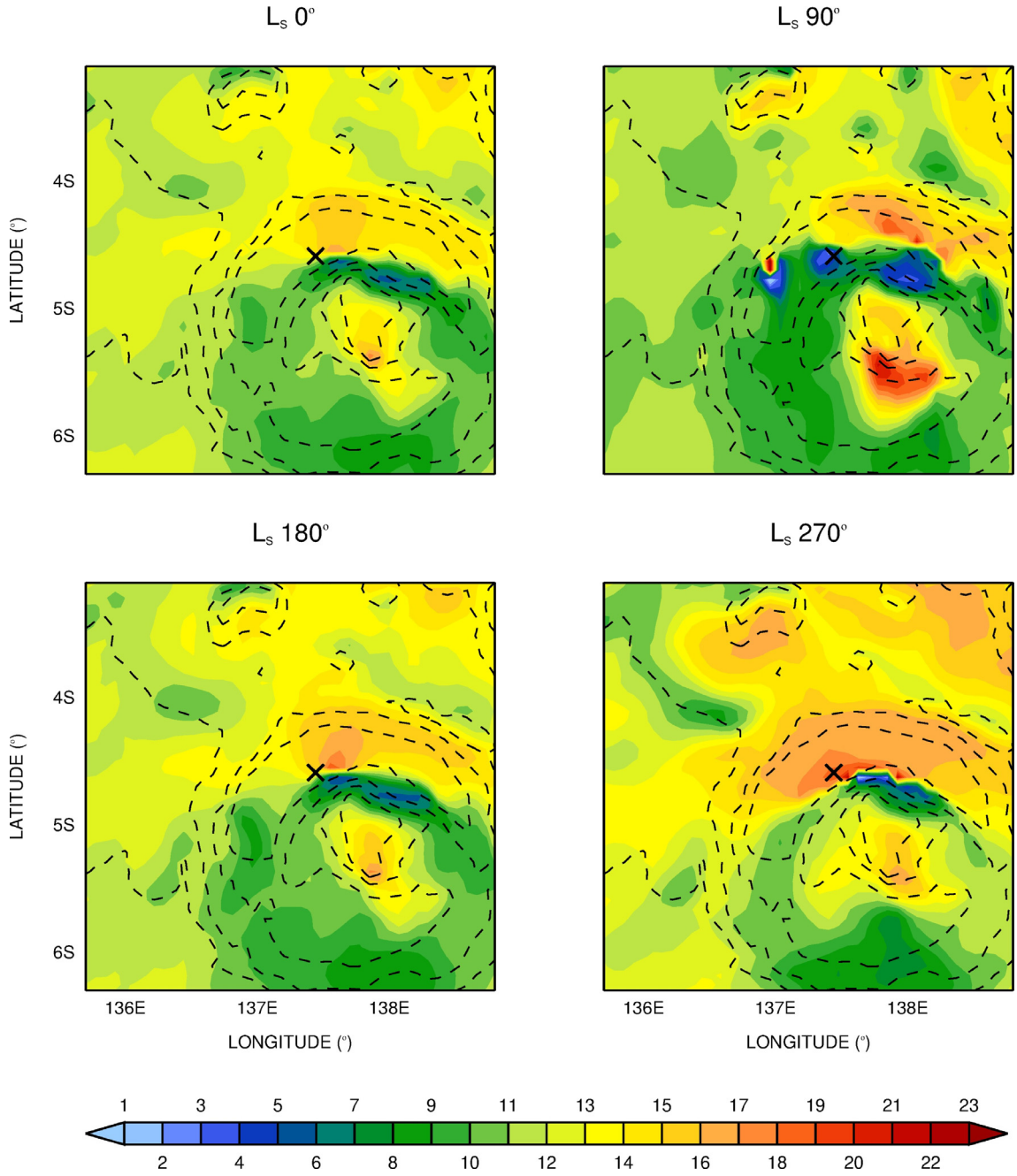

Fig. 10. As Fig. 8 but for the time of transition from southerly to northerly winds (in LMST).

5.1. Variability of the boundary layer depth and potential implications for dust mixing

Fig. 12 shows the boundary layer depth for the sols of each of the L_s 0°, 90°, 110°, 180°, 270° and 315° experiments. On the top left of each plot the number of hours when the depth of the PBL exceeds the height of the crater rim (~4.501 km, shown by a black solid line) for each sol is given with the average number of hours for all sols shown in Table 3. All fields are plotted in Local Mean Solar Time (LMST) which differs from Local True Solar Time (LTST) by as much as +0.82 h (around +49 min) at L_s 315° to −0.66 h (around −40 min) at L_s 180°. Fig. 13 shows the maximum boundary layer depth for the sols of the MarsWRF experiments as well as the estimated PBL depth from REMS measurements taken from Moore et al. (2016). The latter is computed in the following way: first the *m* parameter (a non-dimensional parameter that is related to the convective heat transfer coefficient measured by the REMS air temperature sensor and available on a second by second basis) is used to infer the times when there are periodic changes in the wind from late morning to mid-afternoon (roughly between 13:00 to 16:00 LTST) when the convective boundary layer is most active. Following Spiga et al. (2012), the width of the PBL convective cells is assumed to approximately scale with the PBL depth meaning that if the convective cells are assumed to be regular and do not change structure when advected by the wind, the product of their period with the average wind speed can be taken as a rough estimate of the PBL depth. As discussed in Spiga et al. (2012) this approach is found to work well for arid regions on Earth where the period of the surface pressure fluctuations is used instead of the m-modulation period. It is important to stress that the esti-

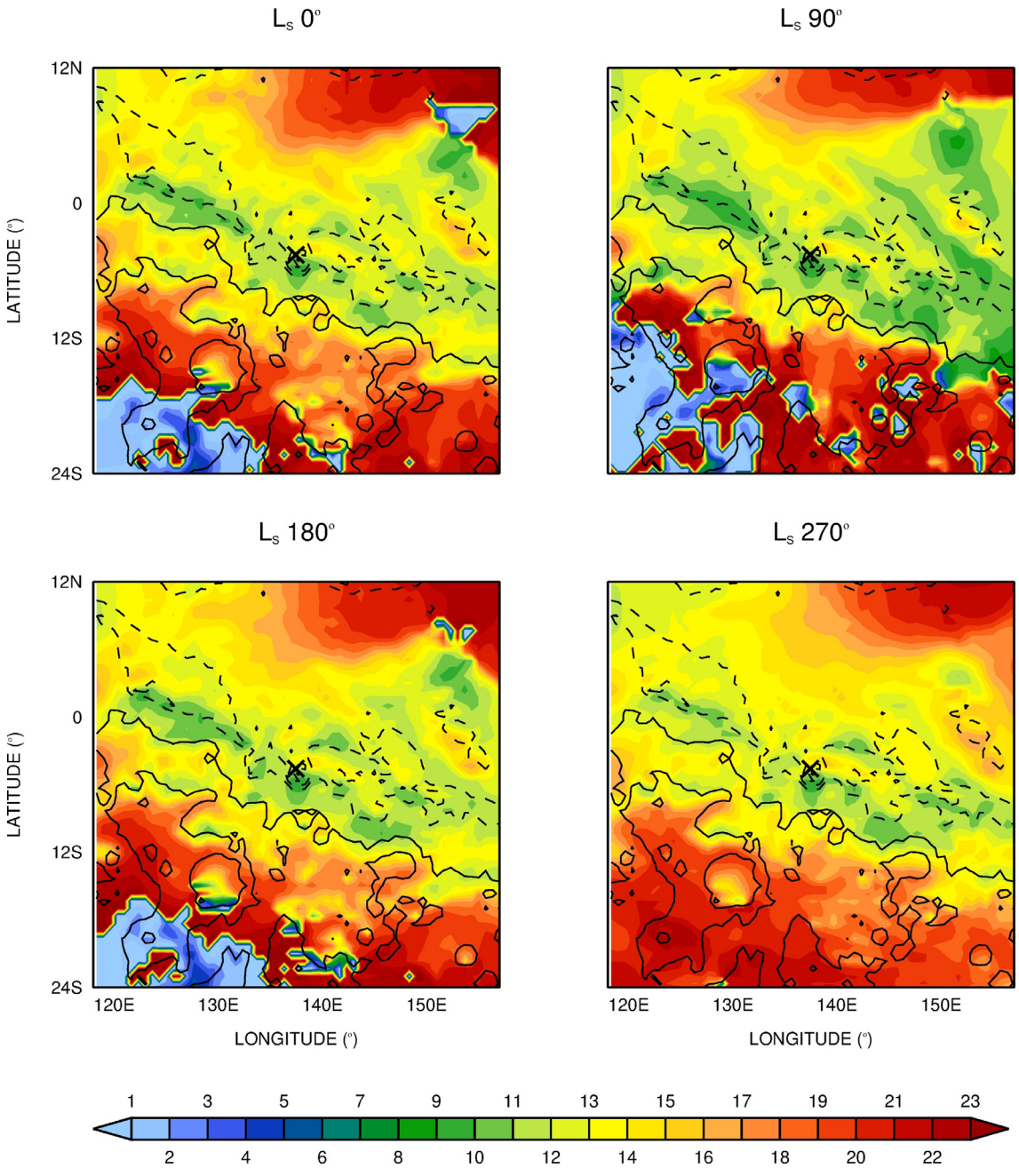

Fig. 11. As Fig. 10 but for model grid #2 (horizontal resolution of ~39.44 km).

Table 3
Average number of hours per sol during which the depth of the PBL exceeds the height of the crater rim for the sols of the L_s 0°, 45°, 90°, 110°, 148°, 180°, 225°, 270° and 315° experiments. Also shown is the mean difference between Local Mean Solar Time (LMST) and Local True Solar Time (LTST) estimated using data available in the REMS files.

Season (L_s)	Number of hours per sol when PBL depth exceeds height of crater rim (h)	LMST – LTST (h)
0°	1.54	0.66
45°	0.00	0.17
90°	0.00	−0.26
110°	0.00	−0.35
148°	0.00	−0.54
180°	1,59	−0.66
225°	1.81	−0.46
270°	3.64	0.26
315°	1.95	0.82

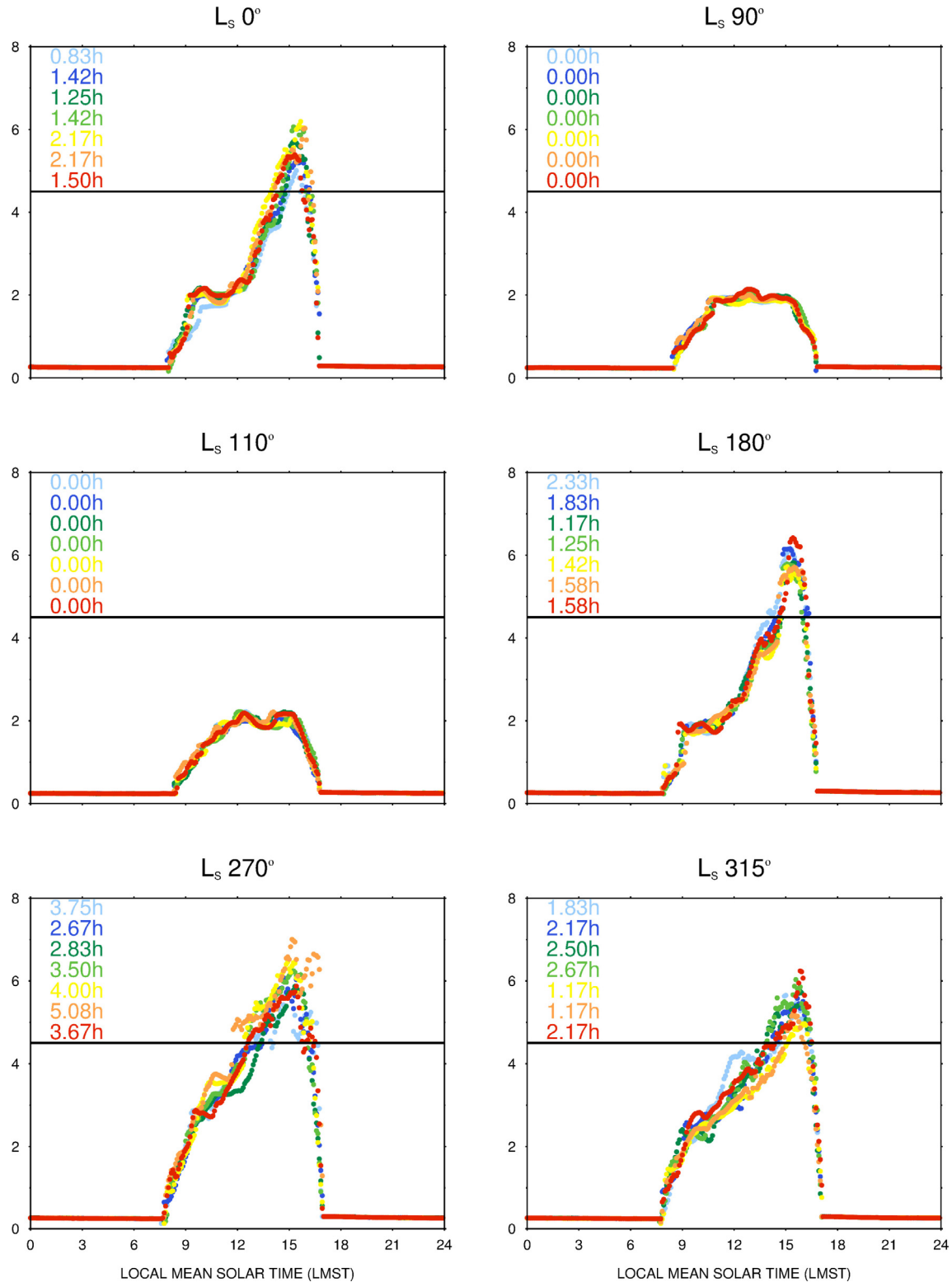

Fig. 12. Planetary Boundary Layer (PBL) depth for the 7 sols (from sol #1 in light blue to sol #7 in red) of the WRF L_s 0°, 90°, 110°, 180°, 270° and 315° experiments. The solid black line represents the height of the crater rim (4.501 km) and the numbers at the top left of each plot are the number of hours in each sol when the boundary layer depth exceeds this height.

mated values of PBL depth should not be directly compared to the MarsWRF-predicted values. REMS data will be more sensitive to rapid local wind variations and to the particular dust loading profile at that specific year and site. For example, the passage of a dust front around REMS/MSL sol 664 was coincident with (a) an increase of the dust devil activity and (b) a sudden rise of the derived PBL depth. On the contrary, MarsWRF averages the behaviour over a grid box and is run with a prescribed dust scenario. In any case it is remarkable that the order of magnitude of both the lower and upper bounds of the PBL depths are comparable using either

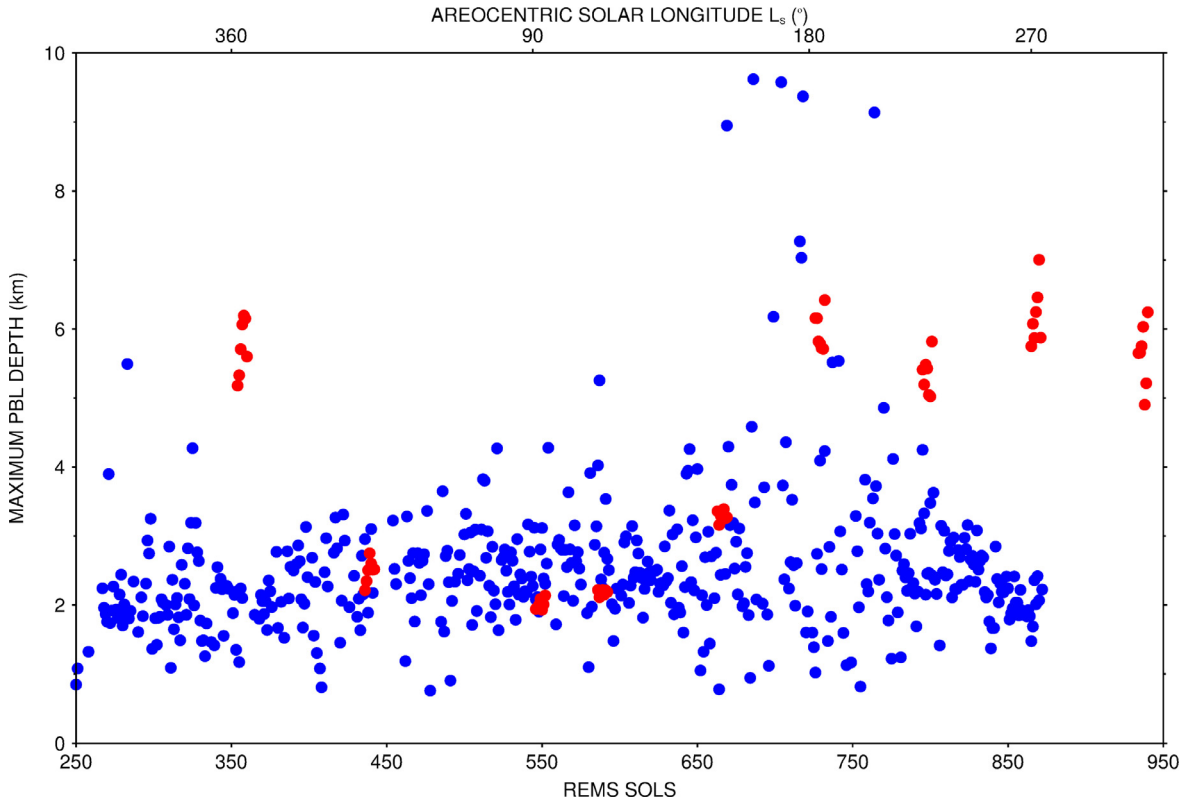

Fig. 13. (Red) maximum Planetary Boundary Layer (PBL) depth (units of km) for the sols of the L_s 0°, 45°, 90°, 110°, 148°, 180°, 225°, 270° and 315° MarsWRF experiments and (blue) boundary layer depth estimated from REMS data for REMS/MSL sols 250 to 873 taken from Moore et al. (2016).

method, although the specific seasonal variability may depend on the dust loading and local weather phenomena.

For the L_s 45°, 90°, 110° and 148° seasons (mid-autumn to mid-spring in the southern hemisphere) the boundary layer depth does not exceed the height of the crater rim for any of the sols with rather shallow depths that do not rise above 2–3 km. Conversely, at the austral summer solstice, L_s 270°, the boundary layer depth exceeds the height of the crater rim by on average 3.64 h per sol with the maximum depths in the range of 5–7 km. From mid-spring to mid-autumn at Gale Crater (warm season), the PBL depth diurnal variability is similar to that predicted by Haberle et al. (2013) at the Viking Lander sites but with higher maximum depths consistent with the fact that Gale is located near the equator experiencing warmer daytime temperatures. While the depth of the nocturnal boundary layer is fairly constant and typically does not exceed 500 m (at night a sharp thermal inversion develops irrespective of the season as a result of the strong radiative cooling of the surface leading to a strongly stratified atmospheric boundary layer), the daytime convective boundary layer deepens in time with the maximum depth occurring normally in the late afternoon just before sunset whereas during most of the daytime hours the PBL is confined to the depth of the crater. These findings are consistent with the findings of Tyler and Barnes (2013) and Rafkin et al. (2016) which showed that the daytime boundary layer at northern Gale Crater is suppressed as a result of the descending motion associated with the upslope flows along the northern crater rim and Mount Sharp. The results given in Fig. 12 suggest that it may be of interest to have further measurements in the time period ~14:30–16:30 LMST when, in the warm season, the PBL depth is likely to exceed the height of the crater rim. A close inspection of the boundary layer diurnal cycle reveals that the growth of the convective boundary layer is not steady in time, in particular for some of the sols at L_s 0° and 180° there is a slowdown around ~9–10 LMST with the PBL depth increasing again after ~12 LMST. It is interesting to note that during the referred time the horizontal wind speed reaches a maximum, as seen in Fig. 7, indicating enhanced mixing which seems to reduce the rate of increase of the air temperature (Fig. 5) and hence may explain the slowdown in the PBL growth. During the dust storm season the local circulation at Gale is disrupted by the global mean meridional circulation. At this time of the year the air at the bottom of the crater is likely to be strongly mixed with the outside air (Rafkin et al., 2016) which is only possible if the convective daytime boundary layer is deeper and longer lasting.

Regarding the comparison of the PBL depths predicted by MarsWRF with those estimated from REMS measurements, and bearing in mind the caveats stated before, Fig. 13 shows that they are of a comparable magnitude for the full period. The model-predicted depths are slightly higher at L_s 0° but clearly larger at L_s 270° (the over-estimation of the daytime air and ground temperatures by MarsWRF, seen in Figs. 4 and 5, and the resulting more active convective boundary layer can explain the higher depths in the model) whereas the rather high boundary layer depths of ~9–10 km around L_s 148° occur right after the single event of high dust devil activity which, as discussed before, is not simulated by the model. It is important to note that as MarsWRF is not run with the observed dust distribution (as well as surface properties such as albedo and thermal inertia) for this particular MY, some of the observed sol-to-sol variability in the PBL depth will not be simulated by the model. The PBL depths here are only plotted for the model grid-point closest to the location of the rover but similar values are obtained in most of the northern and north-western sections of Gale between Mount Sharp and the northern crater rim for all seasons (Fig. S2). As a result, the PBL depths given in Fig. 13 can be considered representative of that region of the crater.

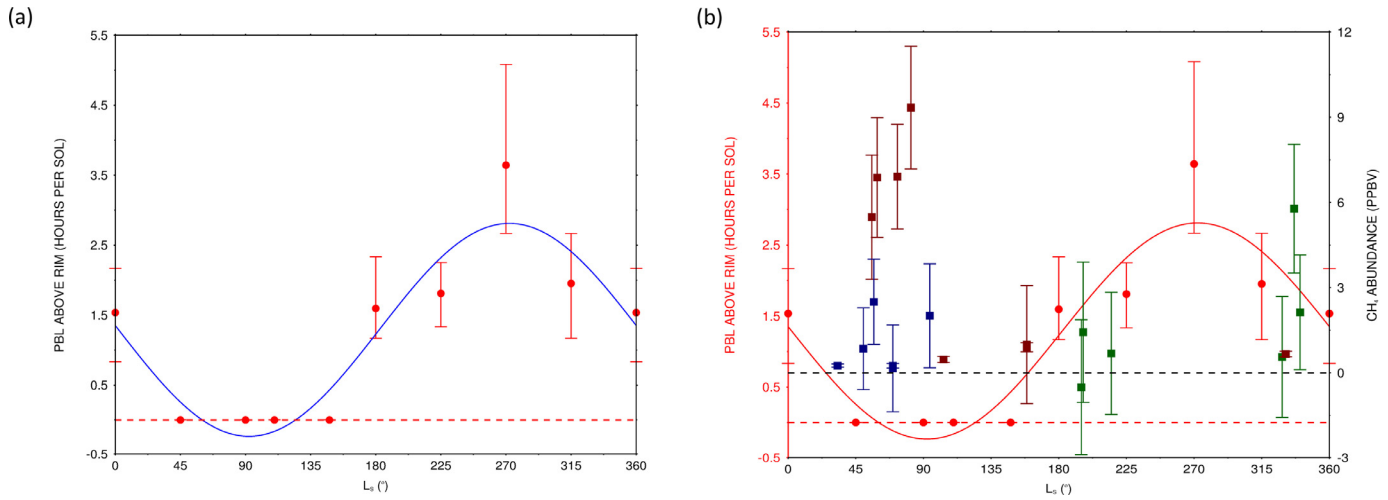

Fig. 14. (a) Average number of hours per sol during which the depth of the PBL exceeds the height of the crater rim (4.501 km) for the sols of the L_s 0°, 45°, 90°, 110°, 148°, 180°, 225°, 270° and 315° WRF experiments (the red dots represent the mean values and the error bars the range for the seven sols of each experiment; the blue curve is a sinusoidal fit to the data). (b) is as (a) but with the methane measurements taken from Webster et al. (2015) added as squares with the correspondent uncertainty. The green, brown and blue squares represent measurements taken in MY31, 32 and 33, respectively.

Fig. 14(a) shows the mean (circles) and the minimum and maximum (range) time periods during which the boundary layer depth exceeds the height of the crater rim for the seven sols of each of the 9 MarsWRF experiments. The blue curve is a sinusoidal fit to the data. In general the higher the mean value the larger the range of values for a given season with a sharp contrast between the austral winter (when this figure is 0 h for all the sols) and summer (when the PBL depth at the location of the rover can exceed the height of the crater rim by more than 5 h in a sol) seasons. As is the case for the PBL depths these values are predicted by the model not just at the grid-point closest to the location of the rover but over the northern and north-western Gale Crater floor (Fig. S3). Moore et al. (2016) shows in their Fig. 2 the line-of-sight extinction, a measure of the amount of dust in the lower layers of the atmosphere. It has a somewhat sinusoidal variability with the lowest values occurring between L_s 90° and 120° and the highest between L_s 270° and 315°. The line-of-sight extinction within the crater is less than the column extinction, a measure of the dust in the whole vertical column, for the majority of the Martian year. This implies that the relatively low mixing ratio of dust within the crater, when compared to the atmosphere above the crater rim, persists throughout most of the year. Furthermore, even though the line-of-sight extinction and the column extinction (opacity) have different yearly trends, the data do show a convergence of the two around L_s 270°–315°. This suggests that at this time of the year the air above the crater mixes with air inside the crater. The results given in Fig. 14(a) show that the average time when the PBL is deeper than the crater rim increases and decreases with the same rate and pattern as the line-of-sight of dust within the crater and that the season when maximal (minimal) mixing is produced is L_s 270°−315° (L_s 90°−110°). This suggests that the PBL height and time duration variations is a possible mechanism that may account for the observed changes in dust mixing within the crater.

5.2. Implications for the variability of trace gases

In the previous section it is shown that variations in the depth of the boundary layer, and the time during which it exceeds the height of the crater rim, may be one of the drivers behind the observed changes in dust mixing within the crater. It therefore seems likely that the variability in the PBL depth may also account for some of the changes of other trace molecules that are sensed at the surface such as methane. In Fig. 14(b) the Curiosity Tunable Laser Spectrometer (TLS) – Sample Analysis at Mars (SAM) methane measurements from MY31 to 33 taken from Webster et al. (2015) are plotted on top of the number of hours the PBL depth exceeds the height of the crater rim for all MarsWRF experiments. Although the match is not perfect overall the highest methane measurements take place around the austral winter solstice (L_s 90°), when the boundary layer at Gale is suppressed and confined mostly to the depth of the crater. By contrast, when the PBL is deeper and the air at the bottom of the crater mixes more strongly with the outside air, around the austral summer solstice (L_s 270°), lower amounts of methane have been recorded by Curiosity. This suggests that the two fields are generally anti-correlated pointing towards a local source of methane within the crater. Similar results are obtained for a comparison with the PBL depth (not shown). It is important to stress that there are other factors at play not considered here: as discussed in Webster et al. (2015), methane can be advected from some other location inside the crater (recent modelling work highlighted the crucial role of advection by the wind on the evolution of methane concentrations; Mischna et al., 2011; Viscardy et al., 2016), released by the regolith (it is possible that more favourable conditions for desorption from the regolith exist around the austral winter solstice), produced by degradation of meteoritically delivered organics (a possible mechanism according to Keppler et al. (2012) but unlikely according to Roos-Serote et al. (2016)) or UV degradation of surface organics (e.g. Poch et al., 2014). The results presented in this section simply argue that mixing with the outside air through changes in the depth and temporal extension of the convective boundary layer may account for some of the observed variability of the measured methane concentrations at Gale Crater. These findings also apply to other gases and non-condensables that may be present at the bottom of the crater.

As stated in Webster et al. (2015), all the methane measurements were taken at night except two (MY 31, L_s 336.5°; MY 32, L_s 81.7°) which showed higher values than their closest nighttime counterparts but with a large uncertainty. Hence, and assuming that the methane was advected from elsewhere in the crater, it is important to check how different the nighttime circulation is between the two solstices. Fig. 15(a) shows vertical cross-sections of meridional wind and potential temperature averaged over nighttime hours (~20–04 LMST, as seen in Fig. 12 during this period

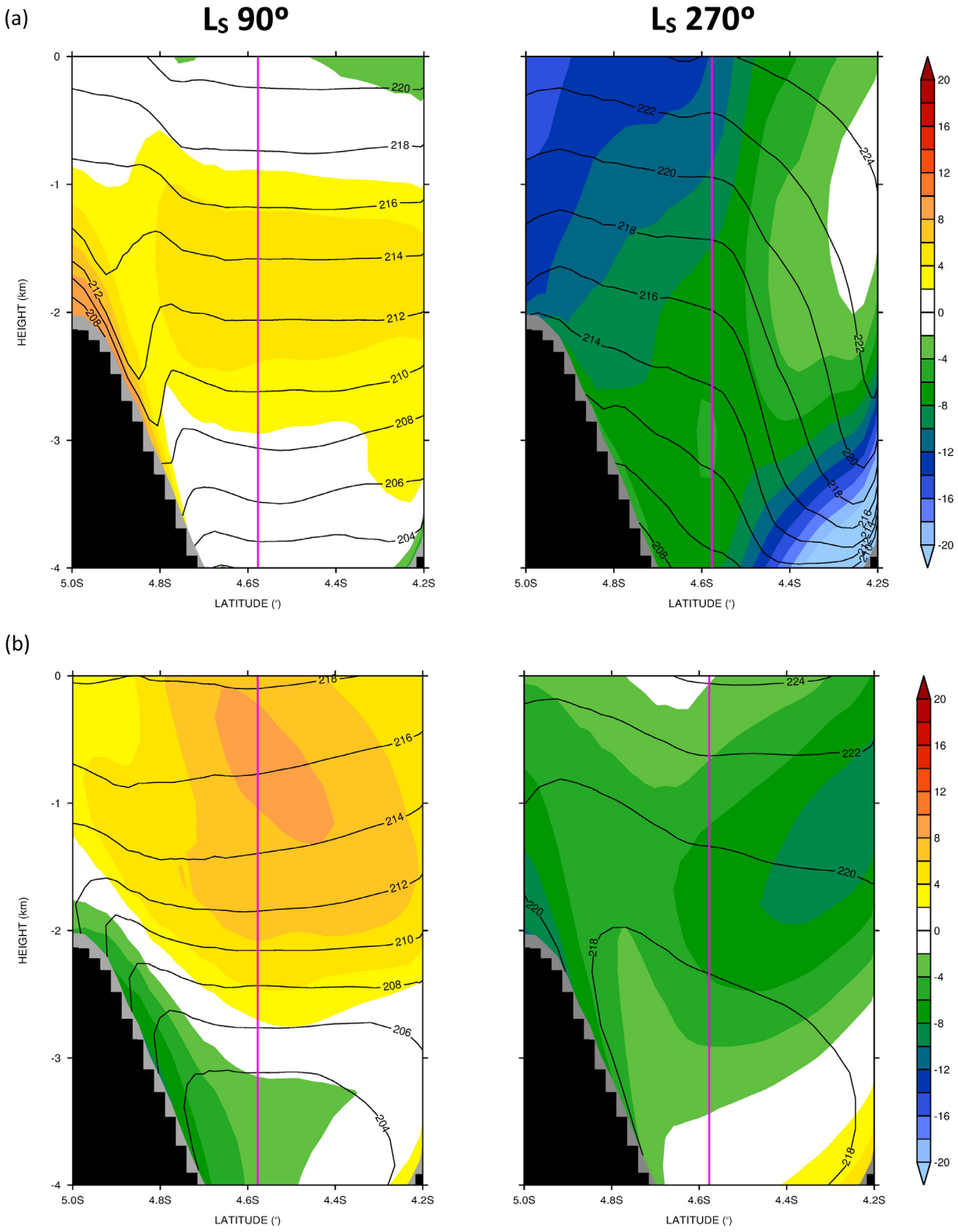

Fig. 15. Vertical cross-section at 137.454°E of potential temperature (solid lines, units of Kelvin, contour interval of 2 K) and meridional wind speed (shading, units of ms^{-1}, contour interval of 2 ms^{-1}) averaged over (a) nighttime hours (~20:00 to 04:00 LMST) and (b) daytime hours (~10:00 to 15:00 LMST) for the sols of the L_s 90° and L_s 270° experiments. Orography as seen by the model is shaded in the black. Regions below the first model level for which there are no data are shaded in grey. The vertical purple line shows the approximate location of Bradbury Landing (~4.58950°S).

nighttime boundary layer dynamics are likely to be at play) for the austral winter (L_s 90°) and summer (L_s 270°) solstices. As can be seen, at L_s 90° the downslope winds from Mount Sharp do not reach the bottom of the crater (as discussed in Rafkin et al. (2016), as they encounter colder air below they lose their negative buoyancy and stop descending) with rather weak winds at Bradbury Landing (even though the rover at this time is located to the south-west of Bradbury Landing there is very little difference in the meridional flow in the region). However, at L_s 270° the meridional wind at the bottom of the crater is large (in excess of 6 m s^{-1} at Bradbury Landing) and from the north with strong downslope winds from the northern crater rim (where speeds exceed 20 ms^{-1}), strengthened by the interaction with the northerly winds from the global mean meridional circulation, extending over the northern section of the crater floor. These results, together with the higher methane measurements around the austral winter solstice, seem to suggest that there could be a methane source located somewhere inside the crater: while in the austral summer season the northerly flow sweeps the crater floor resulting in strong mixing with the outside air and hence lower methane concentrations, in the austral winter season the weak meridional flow allows its concentration to increase at the bottom of the crater.

It was stated before that there are two methane measurements made during the daytime that, even accounting for their large error bars, were very likely higher than their closest nighttime counterparts. They were taken in the late austral summer (MY 31, L_s 336.5°) and autumn (MY 32, L_s 81.7°) seasons with the latter having a larger magnitude and in fact the highest concentration out of all measurements considered here. Fig. 15(b) shows similar vertical cross-sections but for the daytime hours (~10–15 LMST). For both seasons the meridional wind is rather weak: northerly winds with speeds between 2 and 4 m s^{-1} for L_s 90° (likely associated with upslope winds along Mount Sharp) and even weaker winds speeds for L_s 270°. These results appear to convey that there may be a source somewhere to the north of the rover's location, as the weak upslope winds may advect it towards the MSL site. This hypothesis has also been put forward by Webster et al. (2015).

6. Conclusions

In this paper we use MarsWRF to simulate the weather conditions at Gale Crater for about every 45° of solar longitude including the two equinoxes and solstices (L_s 0°, 45°, 90°, 148°, 180°, 225°, 270°) during a Martian year. The model is also run for L_s 110° and L_s 315° as at this time of the year the amount of dust in the lowest levels of the atmosphere at Gale is likely to be near a minimum and maximum, respectively (Moore et al., 2016). As one of the goals of this work is to study the boundary layer dynamics, and given the potential role of mixing with outside air on the variability of dust inside the crater, it is of interest to run the model for those seasons as well. MarsWRF is run with the "MCD MGS" dust scenario (Montmessin et al., 2004; Toigo et al., 2012) that simulates the observed increase in atmospheric opacity during the dust storm season with a maximum just before the austral summer solstice (L_s 270°).

The model is found to generally simulate well the observed surface pressure and air and ground temperatures at Gale for all seasons. For surface pressure the main discrepancies are a higher daily mean value for the sols of L_s 0° and an incorrect simulation of the diurnal variations (the observed maximum and minimum are generally well captured by the model but the diurnal variability is not). These biases are also seen at other locations, such as at the Viking Lander 1 site, suggesting they are most likely due to an incorrect representation of the dust distribution that is critical to get right for the model to properly simulate the diurnal cycle of the surface pressure (Guzewich et al., 2016). For air and ground temperatures the agreement with REMS measurements can be considered very good except at L_s 270° when the daytime ground temperatures are warmer in the model by about 10 K (the air temperatures are on the upper range of the observed values). This can be attributed to an inaccurate representation of the surface properties in particular the albedo which may be too low in the model. This is supported by the fact that the surface albedo at the rover's location used in the model in this season is indeed lower than that estimated by Vasavada et al. (2017). The rate at which the model and REMS air and ground temperatures increase in the morning and decrease in the evening is not the same with the model sometimes warming up slower or faster than observations. As discussed in Pla-Garcia et al. (2016), the most likely reason for this is an incorrect simulation of the topographic orientation, surface properties (such as thermal inertia and albedo) and dust loading. One of the periods for which MarsWRF is run is L_s 148° which comprises REMS/MSL sol 664 when an unusually high number of convective vortices was observed at Gale. The model response does not reveal any unusual features in any of the seven sols of this experiment suggesting that the observed event, likely related to dust storm activity (Kahanpää et al., 2016), is part of the intrinsic natural variability of the real system but not of the model's intrinsic variability as the dust loading is prescribed in MarsWRF. It is important to stress that MarsWRF is run without data assimilation and that the surface properties and dust loading used are not those of MY32 so if there was any forcing in the observations that led to the observed dust devil burst, such as a dust front suggested by Kahanpää et al. (2016), it is not included in the model and hence MarsWRF will not be able to simulate the observed event.

The agreement between the observed and modelled horizontal wind direction and speed is not as good as that obtained for the other fields mentioned above. The large uncertainty in the wind direction, in particular when the wind is blowing from the rear of the rover in which case no wind speed is given (the reason for this is that one of the two wind sensor booms was lost on landing and the measurements given by the other are strongly affected by the Remote Sensing Mast when the wind is blowing from the rear of the rover; more information in Gómez-Elvira et al. (2012) and Newman et al. (2017)) and wind speed (estimated to be ± 20%), together with the fact that the horizontal wind exhibits large high-frequency fluctuations that the model at 1.46 km horizontal resolution is not capable of simulating, mean that it will be harder for MarsWRF to simulate the winds. In addition, the REMS winds are in situ winds averaged over 5-minute periods whereas the MarsWRF's winds are instantaneous winds but effectively 'averaged' over the area of the innermost grid box. Together with the referred larger uncertainty in the observed wind measurements and expected wind variability, a poorer match between the model output and observations (compared to other variables) is to be expected, even if the model were to be relatively accurate. In any case the model captures the easterly to northerly winds from early morning to mid-afternoon, in particular at L_s 270° when they are more persistent, but misses some of the southerly winds in mid-morning and mid to late-afternoon in particular at L_s 180° and 315°. The large variability in the horizontal wind direction in the late afternoon and evening hours in the sols of the L_s 90° and 110° seasons is generally reproduced by the model. MarsWRF successfully simulates the wind speed in the early morning for all seasons but significantly underestimates the late afternoon to evening speeds, in particular for the L_s 90°, 110° and 180° seasons. A possible explanation for the referred biases is the reduced horizontal and vertical resolution of the model grid as well as possible deficiencies in the PBL scheme. Regarding the spatial resolution, a properly representation of the surface properties and topography is needed to simulate the winds as some directions can be blocked by topographic features (Newman et al., 2017). In the referred papers the

authors have also shown that by using a vertical grid with higher resolution near the surface the model gives a better estimate of the shape of the wind speed distribution in the late afternoon and evening but there is a deterioration of the performance in the early morning meaning that the choice of vertical resolution also has an important role on the model-predicted horizontal winds.

In addition to the Hadley Cell, the circulation at Gale Crater is the result of the interaction between regional (including the dichotomy boundary flow and flows from nearby topographic features such as Elysium Mons located to the north) and local (along the crater rims and the slopes of Mount Sharp) slope flows. These slope flows are upslope during daytime and downslope during nighttime hours with the transition between the two regimes taking place at different times meaning that should they interact with each other they will not always do so destructively at the northern crater rim and constructively at the southern crater rim (Tyler and Barnes, 2013). A more comprehensive understanding of how the slope flows along the crater rims and the dichotomy boundary flow interact is achieved here by first removing the daily mean, which will contain the signal from the global mean meridional circulation, and then fitting the meridional wind variations to a sinusoidal function with a period of 24 h. This simple approach allows an estimate of the magnitude and phase of the wind at different locations in the crater as well as the estimation of the approximate transition times between the two regimes for the different seasons. The northern crater floor, including Bradbury Landing and the region over which the rover has been traversing, has one of the smallest magnitudes anywhere in the crater in particular at L_s 90° when it does not exceed 1 m s^{-1}, indicating reduced lateral mixing with the outside air (even though the fit here is done to the meridional wind anomalies, the background meridional wind is rather weak with similar results obtained if the full meridional wind is considered). The largest magnitudes are typically seen at the south-western section of the crater in pre-dawn and late-afternoon hours (here they can exceed 20 m s^{-1}) except at L_s 270° when the highest wind speeds occur in portions of the northern crater rim in late morning and nighttime hours. An analysis of the transition times showed that at the northern crater rim the local crater slope flow switches to downslope mode earlier than the dichotomy boundary flow meaning that in case they interact with each other, which is more likely around L_s 270° and very unlikely around L_s 90°, the interaction will be constructive from late afternoon to nighttime hours (typically between ~17–23 LMST) when the two blow from north to south and in pre-dawn to early morning hours (~5–11 LMST) when they blow from south to north. At the southern crater rim the local slope flow also transitions to a new regime a few hours earlier than the regional slope flow and hence if they interact they will do so destructively in the morning (~10–11 LMST) and at night (~22–23 LMST). In order to determine in which seasons the referred interaction between the crater rim slope flows and the dichotomy boundary flow is more likely to take place, semi-idealised experiments with some of the topographic features smoothed out or even removed have to be performed. These experiments will be discussed in a subsequent paper. This analysis has given further insight into the regions in which lateral mixing with outside air (i.e. mixing with air advected into and out of the crater) could be more likely to occur as well as when stronger slope flows may be expected as a result of a possible interaction between local and regional slope flows. These findings can be extended to similar craters on Mars located at the edge of the hemispheric dichotomy.

Regarding the boundary layer dynamics, there are essentially two regimes at Gale Crater: from mid austral autumn to mid austral spring the PBL is confined within the crater at all times with maximum depths in the range 2–3 km whereas outside this period the convective boundary layer deepens in time with maximum depths of 5–7 km just before sunset. At night and for all seasons the boundary layer is rather shallow, with depths that do not exceed 500 m, as a result of the strong radiative cooling of the surface and subsequent development of a strong thermal inversion. A comparison with the line-of-sight extinction of Moore et al. (2016) suggests that changes in the boundary layer are a key driver of dust mixing within the crater: the time during which the PBL depth exceeds the height of the crater rim is 0 h from L_s 45° to 148° (when the atmosphere near the crater floor is clearer) and peaks at an average of 3.64 h per sol at L_s 270° (when the low-level air is dustier at northern Gale Crater with comparable values of line-of-sight and column extinction indicating strong mixing with the outside air). The deeper and longer lasting convective boundary layer in the austral summer season is therefore consistent with strong mixing with air from outside the crater that is likely to take place at this time (Rafkin et al., 2016). The fact that the PBL at northern Gale is normally confined within the crater except for a few hours in the warm season is also consistent with the findings of Tyler and Barnes (2013). The PBL depths obtained from MarsWRF are also compared to those estimated from REMS data. They are found to be in general agreement with the largest discrepancy occurring in the sols of the L_s 270° experiment in which the model boundary layer depths are larger by ~2–4 km. A possible explanation is that the model daytime air and ground temperatures are higher than those observed by REMS (the ground temperature by up to 10 K) leading to a deeper convective boundary layer. The results of the PBL depth and the time during which the boundary layer exceeds the height of the crater rim described above are at the grid-point closest to the rover location but similar results are predicted by the model at the northern and north-western section of the Gale Crater floor.

In addition to at least partly explaining the observed changes in dust mixing ratio at the bottom of the crater, the variability of the boundary layer depth may also account for some of the changes in the concentration of trace gases such as methane: when the time during which the PBL depth exceeds the height of the crater rim is superimposed on the methane measurements taken by Curiosity given in Webster et al. (2015), a general anti-correlation is seen with higher amounts of methane typically measured around L_s 90° when the convective boundary layer is more suppressed and vice-versa suggesting a possible local source within the crater. Even though, as discussed in Webster et al. (2015), other processes not considered here may also explain the observed variation in methane concentration, mixing with the outside air through changes in boundary layer depth is a possible mechanism that can account for some of the observed variability in the amount of non-condensable and trace gases at the bottom of Gale and other craters on Mars. As stated in Webster et al. (2015), with the exception of two measurements, which are higher than their closest nighttime counterparts but have a large uncertainty, all methane recordings took place at night. An analysis of the model's circulation during nighttime hours indicates a weak meridional flow at the location of Bradbury Landing near L_s 90° and strong northerly winds around L_s 270° that descend along the northern crater rim and sweep the entire crater floor reaching the slopes of Mount Sharp. This is consistent with a local source within the crater as the northerly winds that bring air from outside the crater will act to disperse the gas. During daytime the meridional flow is rather weak with predominantly northerly winds at L_s 90° when the highest methane concentration has been measured. This points to a source somewhere to the north of the MSL site, a hypothesis also raised by Webster et al. (2015).

Curiosity has monitored the dust and methane atmospheric content within a crater close to the equator over multiple seasons. These observations were analysed here in light of the PBL depth variability during different seasons. A comparison with the smooth

variation of the line-of-sight extinction of Moore et al. (2016) suggests that changes in the boundary layer is likely to be a key driver of dust mixing within the crater, whereas the methane measurements showed higher variability within a few sols with ups and downs which may be associated with sudden transient changes in the PBL depth or lateral wind transportation processes. It is important to stress that MarsWRF is not run with the observed dust distribution (as well as surface properties such as albedo and thermal inertia) for this particular MY and hence only intrinsic natural variability is simulated by the model.

In the experiments discussed in this paper MarsWRF is run "dry" . Given that the relative humidity is one of the fields measured by REMS (which can be used for model verification) and recent studies on likely frost events (Martínez et al., 2015) and water activity (Martín-Torres et al., 2015) at Gale, in future simulations the model will be run with an active water cycle. Semi-idealised experiments, in which some orographic features are smoothed out or removed, may yield further insight into the circulation dynamics at Gale Crater whereas idealised experiments with localized methane sources, like those performed by Mischna et al. (2011) but at a higher spatial resolution and centered at Gale, may give a better understanding of the role of the atmospheric circulation on the variability of methane inside the crater. Such experiments will be left to a future study.

Acknowledgements

We are grateful to the MSL science team for their hard work since the beginning of the mission, and in particular, during operations. The simulations presented in this paper were performed on resources provided by the Swedish National Infrastructure for Computing (SNIC) at the High Performance Computing Center North (HPC2N). We would like to thank Claire Newman and an anonymous reviewer for their detailed and insightful comments and suggestions that helped to improve the quality of the paper.

Supplementary materials

Supplementary material associated with this article can be found, in the online version, at doi:10.1016/j.icarus.2017.11.036.

References

Anderson, R.B., Bell III, J.F., 2010. Geological mapping and characterization of Gale Crater and implications for its potential as a Mars Science Laboratory landing site. Mars 5, 76–128.

Clancy, R.T., Sandor, B.J., Wolff, M.J., Christensen, P.R., Smith, M.D., Pearl, J.C., Conrath, B.J., Wilson, R.J., 2000. An intercomparison of ground-based millimeter, MGS TES, and Viking atmospheric temperature measurements: Seasonal and interannual variability of temperatures and dust loading in the global Mars atmosphere. J. Geophys. Res. 105, 9553–9571.

Conrath, B.J., 1975. Thermal structure of the Martian atmosphere during the dissipation of dust torm 1971. Icarus 24, 34–46.

Forget, F., Hourdin, F., Fournier, R., Hourdin, C., Talagrand, O., Collins, M., Lewis, S.R., Read, P.L., Huot, J.-P., 1999. Improved general circulation models of the Martian atmosphere from the surface to above 80 km. J. Geophys. Res. 104, 24155–24175.

Gómez-Elvira, J., Armiens, C., Castañer, L., Domínguez, M., Genzer, M., Gómez, F., Haberle, R., Harri, A.-M., Jiménez, V., Kahanpää, H., Kowalski, L., Lepinette, A., Martín, J., Martínez-Frías, J., McEwan, I., Mora, L., Moreno, J., Navarro, S., de Pablo, M.A., Peinado, V., Peña, A., Polkko, J., Ramos, M., Rennó, N.O., Ricart, J., Richardson, M., Rodríguez-Manfredi, J., Romeral, J., Sebastián, E., Serrano, J., de la Torre Juárez, M., Torres, J., Torrero, F., Urquí, R., Vázquez, L., Velasco, T., Verdasca, J., Zorzano, M.-P., Martín-Torres, J., 2012. REMS: the environmental sensor suite for the mars science laboratory rover. Space Sci. Rev. 170, 583–640.

Gómez-Elvira, J., 2013. Mars Science Laboratory Rover Environmental Monitoring Station RDR. NASA Planetary Data System Data V1.0, LSM-M-REMS-5-MODRDR-V1.0.

Gómez-Elvira, J., Armiens, C., Carrasco, I., Genzer, M., Gómez, F., Haberle, R., Hamilton, V.E., Harri, A.-M., Kahanpää, H., Kemppinen, O., Lepinette, A., Soler, J.M., Martín-Torres, J., Martínez-Frías, J., Mischna, M., Mora, L., Navarro, S., Newman, C., de Pablo, M.A., Peinado, V., Polkko, J., Rafkin, S.C.R., Ramos, M., Rennó, N.O., Richardson, M., Rodríguez-Manfredi, J.A., Romeral Planelló, J.J., Sebastián, E., de la Torre Juárez, M., Torres, J., Urquí, R., Vasavada, A.R., Verdasca, J., Zorzano, M.-P., 2014. Curiosity's rover environmental monitoring station: Overview of the first 100 sols. J. Geophys. Res. Planets 119, 1680–1688.

Guo, X., Lawson, W.G., Richardson, M.I., Toigo, A.D., 2009. Fitting the Viking lander surface pressure cycle with a Mars general circulation Model. J. Geophys. Res. 114. doi:10.1029/2008JE003302.

Guzewich, S.D., Newman, C.E., de la Torre Juárez, M, Wilson, R.J., Lemmon, M., Smith, M.D., Kahanpää, H., Harri, A.-M., 2016. Atmospheric tides in Gale Crater, Mars. Icarus 268, 37–49.

Haberle, R.M., Gómez-Elvira, J., de la Torre Juárez, M., Harri, A.-M., Hollingsworth, J.L., Kahanpää, H., Kahre, M.A., Lemmon, M., Martín-Torres, F.J., Mischna, M., Moores, J.E., Newman, C., Rafkin, S.C.R., Rennó, N., Richardson, M.I., Rodríguez-Manfredi, J.A., Vasavada, A.R., Zorzano-Mier, M.-P.REMS/MSL Science Teams, 2014. Preliminary interpretation of the REMS pressure data from the first 100 sols of the MSL mission. J. Geophys. Res. Planets 119, 440–453.

Haberle, R.M., Houben, H.C., Hertenstein, R., Herdtl, T., 2013. A boundary-layer model for Mars: comparison with viking lander and entry data. J. Atmos. Sci. 50, 1544–1559.

Hamilton, V.E., Vasavada, A.R., Sebastián, E., de la Torre Juárez, M., Ramos, M., Armiens, C., Arvidson, E.R., Carrasco, I., Christensen, P.R., de Pablo, M.A., Goetz, W., Gómez-Elvira, J., Lemmon, M.T., Madsen, M.B., Martín-Torres, F.J., Martínez-Frías, J., Molina, A., Palucis, M.C., Rafkin, S.C.R., Richardson, M.I., Yingst, R.A., Zorzano, M.-P., 2014. Observations and preliminary science results from the first 100 Sols of MSL REMS ground temperature sensor measurements at Gale Crater. J. Geophys. Res. Planets 119, 745–770.

Hong, S.-Y., Pan, H.-L., 1996. Nonlocal boundary layer vertical diffusion in a medium-range forecast model. Mon. Wea. Rev. 124, 2322–2339.

Hourdin, F., Van, P.L., Forget, F., Talagrand, O., 1993. Meteorological variability and the annual surface pressure cycle on Mars. J. Atmos. Sci. 50, 3625–3640.

Jiménez, P.A., Dudhia, J., González-Rouco, J.F., Navarro, J., Montávez, J.P., García-Bustamante, E., 2012. A revised scheme for the WRF surface layer formulation. Mon. Weather Rev. 140, 898–918.

Joshi, M.M., Lewis, S.R., Read, P.L., Catling, D.C., 1995. Western boundary currents in the Martian atmosphere: Numerical simulations and observational evidence. J. Geophys. Res. 100, 5485–5500.

Keppler, F, Vigano, I, McLeod, A, Ott, U, Früchtl, M, Röckmann, T, 2012. Ultraviolet-radiation-induced methane emissions from meteorites and the martian atmosphere. Nature 486, 93–96.

Kahanpää, H., Newman, C., Moores, J., Zorzano, M.-P., Martín-Torres, J., Navarro, S., Lepinette, A., Cantor, B., Lemoon, M.T., Valentín-Serrano, P., Ullán, A., Schmidt, W., 2016. Convective vortices and dust devils at the MSL landing site: Annual variability. J. Geophys. Res. Planets 121, 1514–1549.

Lopez-Valverde, M.A., Haberle, R.M., Lopez-Puertas, M., 2000. Non-LTE radiative mesospheric study for Mars pathfinder entry. Icarus 146, 360–365.

Martín-Torres, J., Zorzano, M.-P., Valentín-Serrano, P., Harri, A.-M., Genzer, M., Kemppinen, O., Rivera-Valentin, E.G., Jun, I., Wray, J., Bo Madsen, M., Goetz, W., McEwen, A.S., Hardgrove, C., Rennó, N.O., Chevrier, V.F., Mischna, M., Navarro-González, R., Martínez-Frías, J., Conrad, P., McConnochie, T., Cockell, C., Berger, G., Vasavada, A.R., Summer, D., Vaniman, D., 2015. Transient liquid water and water activity at Gale Crater on Mars. Nat. Geosci. 8, 357–361.

Martínez, M., Rennó, N.O., Fischer, E., Borlina, C.S., Hallet, B., de la Torre Juárez, M., Vasavada, A.R., Ramos, M., Hamilton, V., Gómez-Elvira, J., Haberle, R.M., 2014. Surface energy budget and thermal inertia at Gale Crater: Calculations from ground-based measurements. J. Geophys. Res. Planets 119, 1822–1838.

Martínez, M., Fischer, E., Rennó, N.O., Sebastián, E., Kemppinen, O., Bridges, N., Borlina, C.S., Meslin, P.-Y., Genzer, M., Harri, A.-M., Vicente-Retortillo, A., Ramos, M., de la Torre Juárez, M., Goméz, F., Goméz-Elvira, J.The REMS Team, 2015. Likely frost events at Gale Crater: analysis from MSL/REMS measurements. Icarus doi:10.1016/j.icarus.2015.12.004.

McCleese, D.J., Heavens, N.G., Schofield, J.T., Abdou, W.A., Banfield, J.L., Calcutt, S.B., Irwin, P.G.J., Kass, D.M., Kleinböhl, A., Lewis, S.R., Paige, D.A., Read, P.L., Richardson, M.I., Shirley, J.H., Taylor, F.W., Teanby, N., Zurek, R.W., 2010. Structure and dynamics of the Martian lower and middle atmosphere as observed by the Mars climate sounder: seasonal variations in zonal mean temperature, dust, and water ice aerosols. J. Geophys. Res. 115, E12016. doi:10.1029/2010JE003677.

Mischna, M.A., Allen, M., Richardson, M.I., Newman, C.E., Toigo, A.D., 2011. Atmospheric modelling of Mars methane surface release. Planet Space Sci 59, 227–237.

Mischna, M.A., Lee, C., Richardson, M.I., 2012. Development of a fast, accurate radiative transfer model for the Martian atmosphere, past and present. J. Geophys. Res. Planets 117, E10009. doi:10.1029/2012JE004110.

Montmessin, F., Forget, F., Rannou, P., Cabane, M., Haberle, R.M., 2004. Origin and role of water ice clouds in the Martian water cycle as inferred from a general circulation model. J. Geophys. Res. Planets 109 (E10004). doi:10.1029/2004JE002284.

Moore, C.A., Moores, J.E., Lemmon, M.T., Rafkin, S.C.R., Francis, R., Pla-García, J., Haberle, R.M., Zorzano, M.-P., Martín-Torres, F.J., Burton, J.R.The MSL Science Team, 2016. A full Martian year of line-of-sight extinction within Gale Crater, Mars as acquired by the MSL Navcam through sol 900. Icarus 246, 102–108.

Moores, J.E., Lemmon, M.T., Kahanpää, H., Rafkin, S.C.R., Francis, R., Pla-García, J., Bean, K., Haberle, R., Newman, C., Mischna, M., Vasavada, A.R., de la Torre Juárez, M., Rennó, N.O., Bell, J., Calef, F., Cantor, B., Mcconnochie, T.H., Harri, A.-M., Genzer, M., Wong, M.H., Smoth, M.D., Martín-Torres, F.J., Zorzano, M.-P., Kemppinen, O., McCulloug, E., 2015. Observational evidence of a suppressed planetary boundary layer in northern Gale Crater, Mars as seen by the Navcam instrument onboard the Mars Science Laboratory rover. Icarus 249, 129–142.

Navarro, T., Forget, F., Millour, E., Greybush, S.J., 2014. Detection of detached dust layers in the Martian atmosphere from their thermal signature using assimilation. Geophys. Res. Lett. 41, 6620–6626.
Newman, C.E., Gómez-Elvira, J., Marin, M., Navarro, S., Torres, J., Richardson, M.I., Battalio, J.M., Guzewich, S.D., Sullivan, R., de la Torre, M., Vasavada, A.R., Bridges, N.T., 2017. Winds measured by the Rover Environmental Monitoring Station (REMS) during the Mars Science Laboratory (MSL) rover's Bagnold Dunes Campaign and comparison with numerical modelling using MarsWRF. Icarus 291, 203–231.
Newman, C.E., Richardson, M.I., 2015. The impact of surface dust source exhaustion on the Martian dust cycle, dust storms and interannual variability, as simulated by the MarsWRF general circulation model. Icarus 257, 47–87.
Poch, O, Kaci, S, Stalport, F, Szopa, C, Coll, P, 2014. Laboratory insights into the chemical and kinetic evolution of several organic molecules under simulated Mars surface UV radiation conditions. Icarus 242, 50–63.
Petrosyan, A., Galperin, B., Larsen, S.E., Lewis, S.R., Määttänen, A., Read, P.L., Rennó, N., Rogberg, L.P.H.T., Savijärvi, H., Siili, T., Spiga, A., Toigo, A., Vázquez, L., 2011. The Martian atmospheric boundary layer. Rev. Geophys. 49, RG3005.
Pla-García, J., Rafkin, S.C.R., Kahre, M., Gómez-Elvira, J., Hamilton, V.E., Navarro, S., Torres, J., Marín, M., Vasavada, A., 2016. The Meteorology of Gale Crater as determined from rover environmental monitoring station observations and numerical modeling. Part I: Comparison of model simulations with observations. Icarus 280, 103–113.
Putzig, N.E., Mellon, M.T., 2007. Apparent thermal inertia and the surface heterogeneity of Mars. Icarus 191, 68–94.
Rafkin, S.C.R., Pla-García, J., Kahre, M., Gómez-Elvira, J., Hamilton, V.E., Marín, M., Navarro, S., Torres, J., Vasavada, A., 2016. The meteorology of Gale Crater as determined from rover environmental monitoring station observations and numerical modeling. Part II: interpretation. Icarus 280, 114–138.
Richardson, M.I., Toigo, A.D., Newman, C.E., 2007. PlanetWRF: a general purpose, local to global numerical model for planetary atmospheric and climate dynamics. J. Geophys. Res. 112, E09001. doi:10.1029/2006JE002825.
Richardson, M.I., Wilson, R.J., 2002. Investigation of the nature and stability of the Martian seasonal water cycle with a general circulation model. J. Geophys. Res. 107 (E5), 5031. doi:10.1029/2001JE001536.
Ringrose, T.J., Patel, M.R., Towner, M.C., Balme, M., Metzger, S.M., Zarnecki, J.C., 2007. The meteorological signatures of dust devils on Mars. Planet. Space Sci. 55 (14), 2151–2163.
Roos-Serote, M, Atreya, S.K., Webster, C.R., Mahaffy, P.R., 2016. Cometary origin of atmospheric methane variations on Mars unlikely. J. Geophys. Res. Planets 121, 2109–2119.
Savijärvi, H.I., Harri, A.-M., Kemppinen, O., 2015. Mars Science Laboratory diurnal moisture observations and column simulations. J. Geophys. Res. Planets 120, 1011–1021.
Skamarock, W.C., Klemp, J.B., Dudhia, J., Gill, J., Barker, D.M., Duda, M.G., Huang, X.-Y., Wang W., Powers, J.G., 2008. A Description of the Advanced Research WRF version 3, NCAR tech. Note TN-4175_STR, 113.
Smith, D.E., Zuber, M.T., Frey, H.V., Garvin, J.B., Head, J.W., Muhleman, D.O., Pettengill, G.H., Phillips, R.J., Solomon, S.C., Zwally, H.J., Banerdt, W.B., Duxbury, T.C., Golombek, M.P., Lemoine, F.G., Neumann, G.A., Rowlands, D.D., Aharonson, O., Ford, P.G., Ivanov, A.B., Johnson, C.L., McGovern, P.J., Abshire, J.B., Afzal, R.S., Sun, X., 2001. Mars Orbiter Laser Altimeter: Experiment summary after the first year of global mapping of Mars. J. Geophys. Res. 106, 23689–23722.
Spiga, A., 2012. Comment on "Observing desert dust devils with a pressure logger" by Lorenz (2012) - insights on measured pressure fluctuations from large-eddy simulations. Geosci. Instrum. Method. Data Syst. 1, 151–154.
Toigo, A.D., Lee, C., Newman, C.E., Richardson, M.I., 2012. The impact of resolution on the dynamics of the martian global atmosphere: Varying resolution studies with the MarsWRF GCM. Icarus 221, 276–288.
Thompson, B.J., Bridges, N.T., Milliken, R., Baldridge, A., Hook, S.J., Crowley, J.K., Marion, G.M., de Souza Filho, C.R., Brown, A.J., Weitz, C.M., 2011. Constraints on the origin and evolution of the layered mound in Gale Crater, Mars using Mars Reconnaissance Orbiter data. Icarus 214, 413–432.
Tyler, D., Barnes, J., 2013. Mesoscale modelling of the circulation in the Gale Crater region: An investigation into the complex forcing of convective boundary layer depths. Mars 8, 58–77.
Ullán, A., Zorzano, M.-P., Martín-Torres, J., Valentín-Serrano, P., Kahanpää, H., Harri, A.-M., Gómez-Elvira, J., Navarro, S., 2017. Analysis of wind-induced dynamic pressure fluctuations during one and half Martian years at Gale Crater. Icarus 288, 78–87.
Vasavada, A.R., Piqueux, S., Lewis, K.W., Lemmon, M.T., Smith, M.D., 2017. Thermophysical properties along *Curiosity*'s traverse in Gale Crater, Mars, derived from the REMS ground temperature sensor. Icarus 284, 372–386.
Viscardy, S., Daerden, F., Neary, L., 2016. Formation of layers of methane in the atmosphere of Mars after surface release. Geophys. Res. Lett. 43, 1868–1875.
Webster, C.R., Mahaffy, P.R., Atreya, S.K., Flesch, G.J., Mischna, M.A., Meslin, P.-Y., Farley, K.A., Conrad, P.G., Christensen, L.E., Pavlov, A.A., Martín-Torres, J., Zorzano, M.-P., McConnochie, T.H., Owen, T., Eigenbrode, J.L., Glavin, D.P., Steele, A., Malespin, C.A., Douglas Archer Jr., P., Sutter, B., Coll, P., Freissinet, C., McKay, C.P., Moores, J.E., Schwenzer, S.P., Bridges, J.C., Navarro-Gonzalez, R., Gellert, R., Lemmon, M.T.the MSL Science Team, 2015. Mars methane detection and variability at Gale Crater. Science 347, 415–417.
Webster, C.R., Mahaffy, P.R., Atreya, S.K., Flesch, G.J., Farley, K.A.The MSL Science Team, 2013. Low upper limit to Methane Abundance on Mars. Science 342, 355–357.
Wilson, R.J., 1997. A general circulation model of the Martian polar warming. Geophys. Res. Lett. 24, 123–126.
Wilson, R.J., Murphy, J.M., Tyler, D., 2017. Assessing atmospheric thermal forcing from surface pressure data: separating thermal tides and local topographic influence. In: Proceedings of the 6th international workshop on the Mars atmosphere: Modelling and observations. In Granada, Spain held January 17-20.
Zurek R.W., Barnes J.R., Haberle R.M., Pollack J.B., Tillman J.E., Leovy C.B., et al., 1992. Dynamics of the atmosphere of Mars. In: edited by Kieffer H.H., et al. (Eds.), Mars. University of Arizona Press Tucson p. 887.